NeuroImage 187 (2019) 77–92

Contents lists available at ScienceDirect

NeuroImage

journal homepage: www.elsevier.com/locate/neuroimage

Quantifying iron content in magnetic resonance imaging

Kiarash Ghassaban [a], Saifeng Liu [b], Caihong Jiang [c], E. Mark Haacke [a,b,d,*]

[a] Magnetic Resonance Innovations, Inc., Bingham Farms, MI, 48025, USA
[b] The MRI Institute for Biomedical Research, Bingham Farms, MI, 48025, USA
[c] Shanghai World Foreign Language Academy, Shanghai, China
[d] Department of Radiology, Wayne State University, Detroit, MI, 48201, USA

ARTICLE INFO

Keywords:
Magnetic resonance imaging
Iron quantification
Multiple sclerosis
Parkinson's disease
Iron tagged cells
USPIO contrast agents

ABSTRACT

Measuring iron content has practical clinical indications in the study of diseases such as Parkinson's disease, Huntington's disease, ferritinopathies and multiple sclerosis as well as in the quantification of iron content in microbleeds and oxygen saturation in veins. In this work, we review the basic concepts behind imaging iron using T2, T2*, T2′, phase and quantitative susceptibility mapping in the human brain, liver and heart, followed by the applications of in vivo iron quantification in neurodegenerative diseases, iron tagged cells and ultra-small superparamagnetic iron oxide (USPIO) nanoparticles.

Introduction

Iron quantification is an important topic in many clinical applications, such as those related to neurodegenerative diseases and hepatic diseases, since excessive iron is believed to cause damage to the tissue (Stephenson et al., 2014; Pietracupa et al., 2017; St Pierre et al., 2005). It has been shown that iron content in the deep gray matter structures in the brain increases during the normal adult aging process, and excess iron deposition has been observed in several neurodegenerative diseases such as Parkinson's disease (PD) and multiple sclerosis (MS) (Li et al., 2014a; Liu et al., 2016a; Barbosa et al., 2015; Chawla et al., 2016; Chen et al., 2014). Still, for the most part, iron is mainly stored in the liver (Hernando et al., 2014). In the brain, iron (in the form of ferritin) is mainly found in the deep gray matter structures including: the basal ganglia (globus pallidus, putamen and caudate nucleus), midbrain (red nucleus, substantia nigra and subthalamic nuclei) and the dentate nucleus (Haacke et al., 2005). Iron is also found in blood or blood products such as hemoglobin, methemoglobin, hemozoin (in malaria) and hemosiderin (in microbleeds caused by traumatic brain injury (TBI) or stroke) (Haacke et al., 2015; Potchen et al., 2018). Several magnetic resonance imaging (MRI) techniques are available for quantifying in vivo iron content, including various methods based on mapping T2, T2*, T2′, phase and magnetic susceptibility of the tissue (Wang and Liu, 2015; Haacke, 1999; Ma and Wehrli, 1996). The optimal technique for a given clinical application is dependent on the amount or concentration of iron. In this review paper, iron quantification in the brain, liver, heart and in iron-tagged stem cells is discussed.

Theory

Determining T2, T2 and T2′*

The transverse relaxation time, T2, can be determined using data collected with a multi-echo spin echo sequence or multiple single-echo spin echo sequences (Yablonskiy and Haacke, 1997), by modeling the signal at different echo times (TEs) as:

$$S(TE) = \widehat{\rho_0} e^{-TE/T2}\,, \tag{1}$$

where $\widehat{\rho_0}$ is the effective spin density. Similarly, T2* can be determined using data collected with a multi-echo gradient echo sequence, using the same exponential decay model except that T2 is replaced with T2* in Eq. (1). However, when multiple types of tissues with different T2 or T2* values are present in the same pixel, more complex models such as a bi-exponential model may be required. T2′ is defined via $\frac{1}{T2'} = \frac{1}{T2} + \frac{1}{T2'}$ (or R2* = R2 + R2′), and can be obtained by calculating the difference between R2* and R2. This can be done by either estimating T2 and T2* using two separate sequences or by using sequences such as gradient echo sampling of the free induction decay and echo (GESFIDE) or gradient echo sampling of a spin echo (GESSE) to obtain T2 and T2′

* Corresponding author. Department of Radiology, Wayne State University, 3990 John R St., Detroit, MI, 48201, USA.
E-mail address: nmrimaging@aol.com (E.M. Haacke).

https://doi.org/10.1016/j.neuroimage.2018.04.047
Received 23 October 2017; Received in revised form 13 April 2018; Accepted 20 April 2018
Available online 25 April 2018

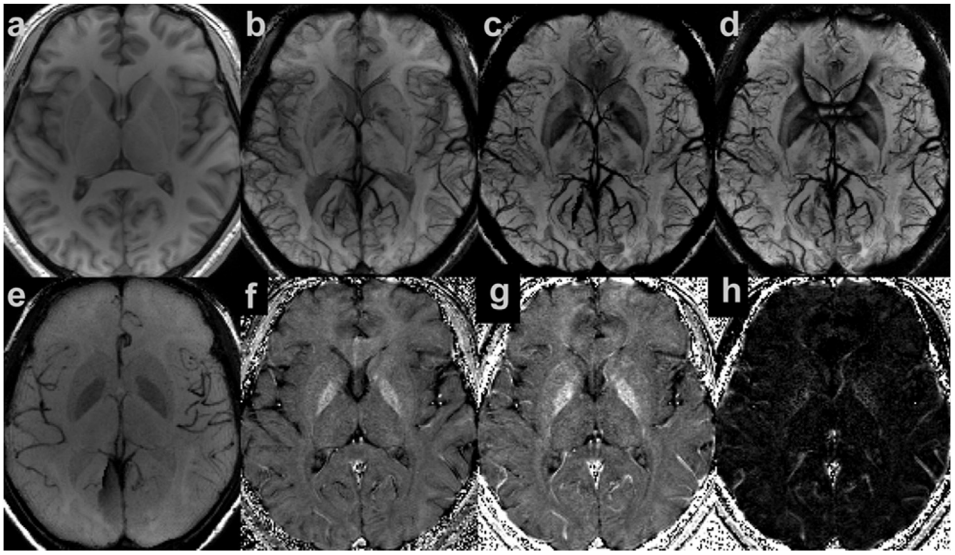

Fig. 1. Post-processed images derived from a gradient echo sampling of the free induction decay and echo (GESFIDE) sequence. (a) T1W image at the first echo; (b) minimum intensity projection (mIP) of the SWI data at TE = 21.04 ms; (c) mIP of the SWI data at TE = 79.66 ms (averaged over 5 echoes from 74.18 ms to 85.14 ms); (d) mIP of the SWI data generated with conventional multi-echo gradient-echo sequence; (e) mIP of the reverse contrast MRA at the spin echo; (f) R2 map; (g) R2* map; (h) R2′ map. The effective slice thickness in (b), (c), (d) and (e) is 16 mm. The SWI data shown in c were generated by first unwrapping the phase images using a multi-echo phase unwrapping algorithm. Hence, the phase aliasing inducing artifacts were removed, compared to the conventional SWI data shown in d. Other imaging parameters included: $B_0 = 3$ T, FOV = 256×192 mm^2; image resolution = $1 \times 1 \times 2$ mm^3; TR = 250 ms, FA = 90/130°; BW = 420 Hz/pixel. Reproduced from Feng et al.'s study (Feng et al., 2013a).

simultaneously (Yablonskiy and Haacke, 1994; Liu et al., 2017a).

However, to do a good job in estimating T2, T2* and T2′, the gradient echo sequence must be run with a high enough resolution, low enough echo time and high enough bandwidth (BW) to minimize dephasing and geometric distortion (Brown et al., 2014). Estimating T2, T2* and T2′ can be done through the GESFIDE sequence along with susceptibility weighted imaging (SWI); some example results are shown in Fig. 1 (Feng et al., 2013a). Once R2′ is measured, the local susceptibility due to sources such as iron, calcium or blood can be found, given the volume fraction of that substance is known, via:

$$R2^{'} = \kappa\lambda\gamma\Delta\chi B_0, \tag{2}$$

where κ is 0.42, λ is the volume fraction, γ is the gyromagnetic ratio, and $\Delta\chi$ is the change in local susceptibility (Yablonskiy and Haacke, 1994). If the source of susceptibility change is capillary blood, then the hematocrit and the level of deoxyhemoglobin would be required to estimate the susceptibility of the blood.

Determining phase

The phase contains key information about the field variations caused either by an imperfect field or by changes in tissue susceptibility (Haacke et al., 2015; Liu et al., 2017a). The phase from a gradient-echo sequence can be written as:

$$\phi(TE) = \gamma\Delta B \cdot TE + \phi_0, \tag{3}$$

for a left-handed system, where ΔB is the field variation and the offset ϕ_0 is related to coil-sensitivity and tissue conductivity (Haacke, 1999). At a given echo time, the more the iron concentration the higher the local field variation and the more rapidly the phase accumulates. In theory, iron concentration can be quantified using local phase information (Haacke et al., 2007). Practically, when imaging the human body, the field variation ΔB can be considered as a combination of the global field variation induced by the air-tissue interfaces and the local field variations induced by tissue susceptibility changes. Usually, the background field components should be removed before the phase images can be used for iron quantification. This is done by using various background field removal algorithms (Liu et al., 2011; Sun and Wilman, 2014; Li et al., 2014b), including high-pass filtering (Haacke et al., 2004), methods based on the spherical mean value properties of harmonic functions (Schweser et al., 2011), as well as solving the background field removal as a Laplacian boundary value problem (Zhou et al., 2014). The advantages and disadvantages are discussed in detail in a few recently published review papers on SWI and quantitative susceptibility mapping (QSM) (Haacke et al., 2015; Wang and Liu, 2015; Liu et al., 2015, 2017a; Reichenbach et al., 2015). It has been shown that the phase shifts correlate with the iron content measured using X-ray fluorescence (XRF) (Hopp et al., 2010). This technique has been used in several studies to quantify cerebral iron content in normal controls and in patients affected by neurodegenerative diseases such as PD and MS (Haacke et al., 2007, 2009, 2010a; Zhang et al., 2010; Wang et al., 2012). However, it is also known that phase can be affected by the orientation of the structures and by imaging parameters such as the main field strength and echo time (Liu et al., 2017a). Fundamentally, since phase is induced by the changes of magnetic susceptibility, it would be better to quantify the source directly, as introduced in the next section.

Determining susceptibility

Magnetic susceptibility is an intrinsic property of any tissue. The susceptibility can be quantified using the following model (Haacke et al., 2015; Wang and Liu, 2015; Liu et al., 2015; Reichenbach et al., 2015):

$$\Delta B_z(\vec{r}) = B_0 \cdot \chi(\vec{r}) * G(\vec{r}), \tag{4}$$

where "*" represents convolution, $\chi(\vec{r})$ is the susceptibility distribution and $G(\vec{r})$ is the point dipole response given as:

$$G(\vec{r}) = \frac{1}{4\pi}\frac{3\cos^2\theta - 1}{r^3}, \tag{5}$$

where θ is the angle between $\vec{r}$ and $\vec{B_0}$. Eq. (4) can be conveniently solved in the Fourier domain. Specifically,

$$G(\vec{k}) = FT(G(\vec{r})) = \frac{1}{3} - \frac{k_z^2}{k^2}, \tag{6}$$

assuming that the main field is in the z direction (Salomir et al., 2003; Cheng et al., 2009). Because of the zeros of $G(\vec{k})$ along the magic angles, quantifying $\chi(\vec{r})$ using Eq. (4) is an ill-posed problem. This problem can be solved by using the straight-forward thresholded k-space division algorithm (Shmueli et al., 2009; Haacke et al., 2010b), or by using more sophisticated algorithms in which the geometries of interest extracted from magnitude, phase and an initial reconstruction of susceptibility maps are utilized as constraints (Liu et al., 2012; Schweser et al., 2012; Tang et al., 2013; Deistung et al., 2017; Bao et al., 2016; Langkammer

et al., 2017). One advantage of using susceptibility for iron quantification, instead of using phase directly, is that susceptibility is not dependent on imaging parameters such as main field strength and echo time (Haacke et al., 2015). Moreover, unlike phase which is orientation dependent, the susceptibility of structures with iron overload (e.g., deep gray matter structures) is generally not dependent on the orientation of the object (Liu et al., 2014, 2017a). Nonetheless, the susceptibility of the white matter can be orientation dependent due to structural and magnetic susceptibility anisotropy (Deistung et al., 2017; Wharton and Bowtell, 2015; Yablonskiy and Sukstanskii, 2017). Finally, and clinically very important, QSM provides information via the sign of the susceptibility as to whether a given structure is paramagnetic (containing more iron) or diamagnetic (containing more calcium).

The relationship between susceptibility and iron content has been investigated in several studies, based on ferritin phantoms and/or post-mortem analyses where the iron content can be verified using XRF and inductively coupled plasma mass spectrometry (ICPMS) (Langkammer et al., 2010; Zheng et al., 2013). Linear relationships between susceptibility and iron content have been shown in earlier studies, with slopes varying from 0.6 to 1.3 ppb/(μgFe per g wet tissue) (Zheng et al., 2013). A recent paper suggests that 1 ppb in susceptibility is equivalent to a value close to 1 μgFe per g wet tissue (Liu et al., 2016a). The variation in the slopes is partly due to the differences in the QSM reconstruction algorithm (Zheng et al., 2013). QSM based iron quantification has been quite successful especially for the basal ganglia, midbrain and dentate nucleus (DN) structures (Li et al., 2014a; Liu et al., 2016a; Barbosa et al., 2015). However, when interpreting the measured susceptibility values in white matter, the contribution of myelin content and susceptibility anisotropy should be considered (Li et al., 2012; Wharton and Bowtell, 2012; Luo et al., 2014; Sukstanskii and Yablonskiy, 2014). A summary of the linear correlations of R2* and QSM with cerebral iron concentration is provided in Table 1. One key point to be aware of is that the coefficient relating susceptibility to iron content will depend on the QSM method and reconstruction parameters.

Other techniques

In addition to the T2, T2*, T2′ and susceptibility mapping based methods introduced above, there are some other techniques which can also be used to measure iron, including T1 mapping, field dependent R2 increase (FDRI) (Bartzokis et al., 1993), magnetic field correlation (MFC) (Jensen et al., 2009), as well as direct saturation based method such as water-saturation shift-referencing (WASSR) (Smith et al., 2009). These methods, although less frequently used due to technical challenges, may provide unique information about tissue properties and can be used as reference methods. For example, compared to T2* mapping, T1 mapping is less susceptible to the field inhomogeneity, and hence, it has the potential to improve both the accuracy and reproducibility of in vivo iron quantification (Sado et al., 2015; Feng et al., 2013b). Ge et al. demonstrated the quantification of iron content in gray matter in multiple sclerosis patients using MFC (Ge et al., 2007). Pfefferbaum et al. compared FDRI with SWI phase imaging for cerebral iron quantification and showed that FDRI has higher specificity to non-heme iron than SWI, despite the fact that FDRI requires data acquired at two different field strengths (Pfefferbaum et al., 2009).

Applications of MRI iron quantification

Quantification of liver iron concentration

Quantification of liver iron concentration (LIC) plays a significant role in the diagnosis and treatment planning for patients with liver iron overload, such as those affected by hereditary hemochromatosis and those who undergo regular blood transfusion (St Pierre et al., 2005; Hernando et al., 2014; Wood et al., 2005a). There are a few ways to measure LIC, including invasive liver biopsy and non-invasive MRI based techniques. We focus on the latter in this review paper. Conventionally, LIC is quantified by measuring the R2 or R2* relaxation rates and then converting them into LICs based on calibration curves determined through liver biopsy. Using R2 mapping at 1.5 T, LICs up to 42 mgFe/g dry tissue were measured (St Pierre et al., 2005). Although the feasibility and effectiveness of R2 mapping based methods have been demonstrated in several studies, there are still a few problems which limit the accuracy and dynamic range of LIC quantification through R2 mapping, such as the non-linear relationships between R2 and LIC (St Pierre et al., 2005; Wood et al., 2005a), long acquisition time of R2 mapping based methods (Wood et al., 2005a), as well as the field strength dependence of the relationships between R2 and LIC (Storey et al., 2007). Most of these problems have been solved by using R2* mapping based methods. As shown by Wood et al. the R2* is linearly related to LIC at 1.5 T according to the relation (Wood et al., 2005a):

$$LIC[c] = 0.0254\left[c/\,s^{-1}\right]\cdot R2^{*}\left[s^{-1}\right] + 0.202[c] \tag{7}$$

where the unit of LIC is mgFe/g dry tissue. In that study, LICs up to 32.9 mgFe/g dry weight were measured using R2* mapping at 1.5 T.

However, there are still a few limitations in LIC quantification using R2* mapping. First, R2* is dependent on the field strength. As shown by Storey et al. the relationship between the R2* obtained at 3 T and 1.5 T is:

$$R2^{*}_{3T}\left[s^{-1}\right] = 2R2^{*}_{1.5T}\left[s^{-1}\right] - R_{d-d}\left[s^{-1}\right], \tag{8}$$

where R_{d-d} is the component related to dipole-dipole interaction and was found to be roughly 11 s^{-1} in the liver (Storey et al., 2007). Second, these relaxation mapping methods require multiple echoes. However, the relatively lower signal-to-noise ratio (SNR) at longer echoes due to R2 or R2* signal decay may limit the dynamic range of these methods. Furthermore, the accuracy of LIC quantification using R2* mapping can be affected by liver fat fraction (Hernando et al., 2013a, 2014). These problems can be addressed by using ultrashort echo times and more sophisticated fitting models which take confounding factors into consideration (Krafft et al., 2016; Yu et al., 2008; Hernando et al., 2013b).

In addition to the popular R2 and R2* mapping based methods for LIC quantification, susceptibility mapping based LIC quantification methods have been proposed (Chu et al., 2004; Taylor et al., 2012; Hernando et al., 2013c; Sharma et al., 2015). These methods include both the simplified model for susceptibility and field variation (Chu et al., 2004; Taylor et al., 2012; Hernando et al., 2013c) and more sophisticated 3D dipole kernel based QSM (Sharma et al., 2015). While the former methods usually measure the field variation induced by the liver iron directly, the latter utilizes the relationship between the susceptibility distribution and field variation which has a simple form in the Fourier domain. In fact, QSM has been shown to be successful in quantifying the cerebral iron content as well as the venous oxygen saturation in many studies and clinical applications (Xia et al., 2014, 2015). It also has superior sensitivity to changes in iron content than R2* mapping (Barbosa et al., 2015; Du et al., 2016). However, the efficacy of QSM for liver iron quantification may be affected by a few factors such as the background field induced by various air-tissue interfaces, the water-fat chemical shift effect and the ill-posed inverse problem in QSM. In a recent study, QSM has been applied to the liver and the susceptibility of the liver was measured with respect to the abdominal fat (Sharma et al., 2015). Although excellent correlation between the liver tissue susceptibility and the liver iron concentration was obtained, the susceptibility of the liver was found to be under-estimated in a follow-up study, in which the susceptibility of the liver estimated by QSM was compared with that of superconducting quantum interference device (SQUID) (Sharma et al., 2017). This is largely due to the relatively low imaging resolution because of the requirement of full liver coverage. The low imaging resolution leads to inaccurate definition of the local field variation and partial volume effects. One way to solve this susceptibility under-estimation problem is to quantify the apparent susceptibility of the

Table 1
Review of studies investigating the linear correlation of R2* and QSM with iron concentration in different brain structures.

Study[a]	Sample Size	Iron Quantification Method	Field Strength (Tesla)	Linear Regression Parameters	Linear Correlation Equation $A \times [Fe] + B$[d]	Brain Structures Included
Yao et al. (2009)	9 HC	R2*	1.5 T	PCC = 0.79, P < 0.01	A = 0.06, B = 1.08	CN, PUT, GP
Ning et al. (2014)	56 Infants	R2*	1.5 T	PCC = 0.75 (CN), PCC = 0.66 (PUT), PCC = 0.67 (GP), P < 0.001	NA	CN, PUT, GP
Uddin et al. (2016)	17 HC	R2*	1.5 T	PCC = 0.85, P < 0.0001	A = 0.06 ± 0.003, B = 12.81 ± 0.42	CN, PUT, GP, RN, SN, THA, FWM, CGM
Martin et al. (2008)	13 HC	R2*	3 T	PCC = 0.91, P = 0.01	NA	CN, PUT, GP, RN, SN, FWM
Peran et al. (2009)	30 HC	R2*	3 T	PCC = 0.96, P < 0.001	A = 0.14, B = 11.31	CN, PUT, GP
Yao et al. (2009)	9 HC	R2*	3 T	PCC = 0.87, P < 0.01	A = 0.12, B = 1.41	CN, PUT, GP
[b] Langkammer et al. (2010)	7 DS	R2*	3 T	PCC = 0.95, P < 0.001	A = 0.27, B = 14.3	CN, PUT, GP, THA, FWM, TWM, OWM
[b] Langkammer et al. (2012a)	6 DS	R2*	3 T	PCC = 0.37, P < 0.01	A = 0.12, B = 22.38	FC, FWM, OC, OWM
Yan et al. (2012)	24 HC	R2*	3 T	PCC = 0.98, P < 0.001	NA	CN, PUT, GP, RN, SN, THA, FWM
Sedlacik et al. (2014)	66 HC	R2*	3 T	PCC = 0.94, P = NA	A = 0.11 ± 0.006, B = 10.69 ± 0.80	CN, PUT, GP
Barbosa et al. (2015)	30 HC	R2*	3 T	PCC = 0.79, P = NA	A = 0.13, B = 20.0	CN, PUT, GP, THA, RN, SN, GM
Uddin et al. (2016)	17 HC	R2*	4.7 T	PCC = 0.95, P < 0.0001	A = 0.196 ± 0.005, B = 16.87 ± 0.71	CN, PUT, GP, RN, SN, THA, FWM, CGM
Yao et al. (2009)	9 HC	R2*	7 T	PCC = 0.92, P < 0.0001	A = 0.32, B = 1.98	CN, PUT, GP
Shmueli et al. (2009)	1 HC	R2*	7 T	PCC = 0.83, P = 0.042	NA	PUT, RN, SN
Bilgic et al. (2012)	23 HC	QSM	1.5 T	PCC = 0.88, P = 0.02	NA	CN, PUT, GP, THA, RN, SN, DN, FWM
Persson et al. (2015)	183 HC	QSM	1.5 T	PCC = 0.97, P < 0.001	A = 0.95, B = −24.50	CN, PUT, GP, THA, RN, SN, DN
Liu et al. (2016a)	174 HC	QSM	1.5 T	PCC = 0.98, P < 0.01	A = 0.89 ± 0.03, B = −48.51 ± 4.09	GP, PUT, THA
Schweser et al. (2011)	5 HC	QSM	3 T	PCC = 0.86, P < 0.001	A = 1.3 ± 0.2[e], B = NA	CN, PUT, GP, THA, RN, SN, DN, FWM
[b] Langkammer et al. (2012b)	13 DS	QSM	3 T	PCC = 0.87, P < 0.001	A = 0.97 ± 0.03, B = −37.0 ± 2.0	CN, PUT, GP, THA, FWM, TWM, OWM
[c] Zheng et al. (2013)	1 MS	QSM	3 T	PCC = 0.87, P = NA	A = 0.80 ± 0.01, B = 10.8 ± 2.9	CN, PUT, GP (Left Hemisphere)
Lim et al. (2013)	5 HC	QSM	3 T	PCC = 0.99, P = NA	A = 0.73, B = −44.15	CN, PUT, GP
Chai et al. (2015)	45 HC	QSM	3 T	PCC = 0.90, P = 0.037	A = 0.55, B = - 18.80	CN, PUT, GP, THA, RN, SN, DN, FWM
He et al. (2015)	35 HC	QSM	3 T	PCC = 0.90, P = 0.007	NA	CN, PUT, GP, RN, SN
Xia et al. (2015)	31 HC	QSM	3 T	PCC = 0.84, P = 0.01	NA	CN, PUT, GP, THA, RN, SN, DN, FWM
Barbosa et al. (2015)	30 HC	QSM	3 T	PCC = 0.83, P = NA	A = 0.65, B = −13.8	CN, PUT, GP, THA, RN, SN. GM
Shmueli et al. (2009)	1 HC	QSM	7 T	PCC = 0.92, P < 0.01	NA	PUT, RN, SN
Wharton and Bowtell (2010)	5 HC	QSM	7 T	PCC = 0.96, P = NA	A = 0.75 ± 0.1, B = NA	CN, PUT, GP, RN, SN, THA, FC

Abbreviations: HC: healthy controls, PCC: Pearson correlation coefficient (R), DS: deceased subjects, PD: Parkinson's disease, CN: caudate nucleus, PUT: putamen, GP: globus pallidus, SN: substantia nigra, RN: red nucleus, THA: thalamus, GM: gray matter, WM: white matter, FWM: frontal white matter, TWM: temporal white matter, OWM: occipital white matter, FC: frontal cortex, OC: occipital cortex, CGM: cortical gray matter, MS: multiple sclerosis, NA: not available.

[a] The in vivo iron concentration was estimated based on the study by Hallgren and Sourander (1958), unless otherwise stated.

[b] The iron concentration in this study was determined using inductively coupled plasma mass spectrometry (ICPMS).

[c] The iron concentration in this study was determined using X-ray Fluorescence (XRF).

[d] For the relationship between R2* and iron, the unit of the slope (A) is s^{-1} per μg Fe/g wet tissue, and the unit of the intercept (B) is s^{-1}. For the relationship between susceptibility and iron, the unit of the slope (A) is ppb per μg Fe/g wet tissue, and the unit of the intercept (B) is ppb.

[e] In this study, the slope was obtained by correcting the contribution of myelin content with magnetization transfer saturation map.

vessels in the liver, by collecting relatively high resolution data without full coverage of the liver (Liu et al., 2016b). Since the apparent susceptibility of the vessel is the difference between the susceptibility of the vessel and the susceptibility of the surrounding liver tissue, it can be used to quantify local LIC in the vicinity of the vessel. As shown in Fig. 2, the apparent susceptibility of the vessels in the liver is positive for a healthy subject and becomes negative for a patient where the liver has high iron content. This is consistent with the higher R2* values of the liver tissue of the patient. Compared to R2* mapping, which requires multi-echo data, QSM can be reconstructed using single-echo data. Additionally, magnetic susceptibility is directly related to iron concentration but is not dependent on field strength. Hence, QSM may help extend the range of quantifiable LICs and has the potential to improve the stability and reproducibility of LIC quantification over R2* mapping. The higher sensitivity of QSM to changes in iron content has been demonstrated in various studies focused on the brain. However, given that the iron concentration is usually much higher in the liver than in the brain and the data processing is much more complicated in QSM than in R2* mapping, the benefit of QSM over R2* mapping still needs to be fully studied.

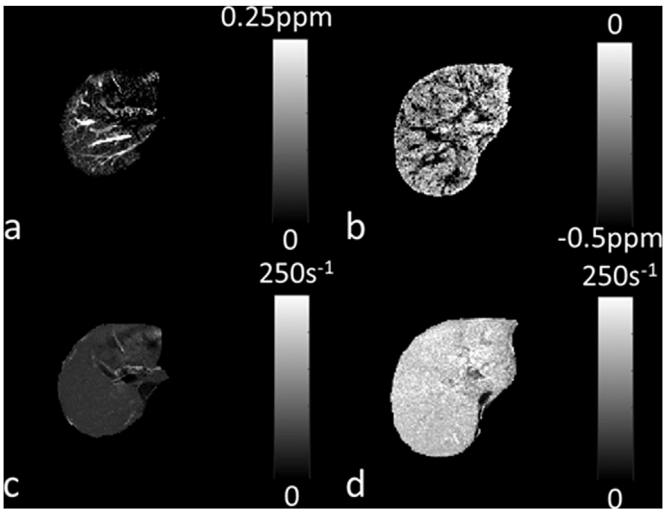

Fig. 2. Quantification of liver iron concentration using QSM. a) Maximum intensity projection (MIP) of QSM data from the liver of a healthy subject. b) Minimum intensity projection (mIP) of QSM data from the liver of a blood-transfusion patient. c) MIP of R2* of the same healthy subject as in a). d) MIP of the R2* data of the patient. The effective slice thickness is 32.4 mm for all the images. With elevated liver iron concentration, the R2* increased, while the apparent susceptibility of the vessels in the liver became negative. Data courtesy of Hongyan Ni, MD (Tianjin First Central Hospital, Tianjin, China).

Quantification of cardiac iron concentration

The quantification of cardiac iron concentration can be of vital importance to the treatment planning for patients undergoing chronic blood transfusion, such as those affected by thalassemia or sickle cell disease, as cardiac iron overload may lead to impaired ventricular function and cardiac failure (Anderson, 2011; Wood, 2014). Although serum ferritin is widely used for monitoring total body iron level, it can be complicated by factors such as inflammation (Anderson, 2011; Wood, 2014). As demonstrated by a few studies, the correlation between serum ferritin and cardiac iron is poor (Fragasso et al., 2011; Anderson et al., 2001). In fact, even the correlation between liver iron concentration and cardiac iron is not reliable (Anderson et al., 2001; Deborah Chirnomas et al., 2008; Wood et al., 2004). For example, patients with high myocardial iron concentration may appear to have low liver iron concentration (Anderson, 2011; Wood, 2014). This partly is due to the differences in the iron clearing kinetics in different organs as well as the patient's chelation history (Anderson, 2011; Deborah Chirnomas et al., 2008). Hence, a direct measurement of the cardiac iron is necessary. This is usually achieved by measuring the T2 and T2* in the myocardium (Anderson, 2011; Wood, 2014; Fragasso et al., 2011; Wood et al., 2004, 2005b). Myocardial T2* has been found to be correlated with the iron in the heart determined through biopsy and postmortem studies (Mavrogeni et al., 2005; Ghugre et al., 2006). At 1.5 T, the cardiac iron concentration can be calculated from R2* as (Carpenter et al., 2011):

$$iron = 0.00985 \cdot R2^{*1.22}, \tag{9}$$

where the unit for iron is mg/g dry weight, and the unit for R2* is s^{-1}. Eq. (9) represents a non-linear relationship between cardiac iron and R2*. If a simple linear model was used instead, using the data presented in the study where Eq. (9) was introduced, the slope of that linear relationship would be roughly 0.032. Comparing with the slope 0.0254 in Eq. (7), which is for the relationship between liver iron and R2* at the same field strength, the consistency in measuring the iron content in different organs using R2* mapping is evident.

Using this method, Carpenter et al. measured myocardial iron up to 25.9 mgFe/g dry weight in patients with severe heart failure at 1.5 T (Carpenter et al., 2011). Typically, a T2* lower than a threshold (20 ms at 1.5 T) is used as an indicator for cardiac iron overload and impaired cardiac function (Anderson, 2011; Wood, 2014). The popularity of T2* mapping is attributed to the availability of software packages for data post-processing and the high sensitivity of T2* to changes in iron content. However, the reliability of T2* can be affected by field inhomogeneity, precisely because of the sensitivity of T2* to susceptibility effects. This can be potentially improved by mapping the T1 and T2 (Sado et al., 2015; Feng et al., 2013b; Wood et al., 2005b). For normal or mild cardiac iron overload, Feng et al. showed that T1 correlated linearly with T2 and T2* in patients with abnormal myocardial iron concentration (Feng et al., 2013b). Additionally, Sado et al. showed that myocardial T1 correlated with the T2* and the T1 mapping based method has better reproducibility than T2* mapping alone (Sado et al., 2015). With the advances in MRI data acquisition sequences and post-processing techniques (Chen et al., 2018; Wang et al., 2018), it may be possible to simultaneously map multiple contrasts. For example, Hamilton et al. showed that T1 and T2 can be simultaneously quantified using MR fingerprinting (Hamilton et al., 2017). These techniques will provide more comprehensive information for diagnosis and treatment planning for patients affected by cardiac iron overload.

Phase and QSM as a means to measure iron content in multiple sclerosis

MS is a demyelinating inflammatory disease often established not just from clinical manifestations of the disease but also using the McDonald criteria for MR imaging which includes the presence of at least two periventricular white matter hyperintensities in T2-weighted (T2W) spin

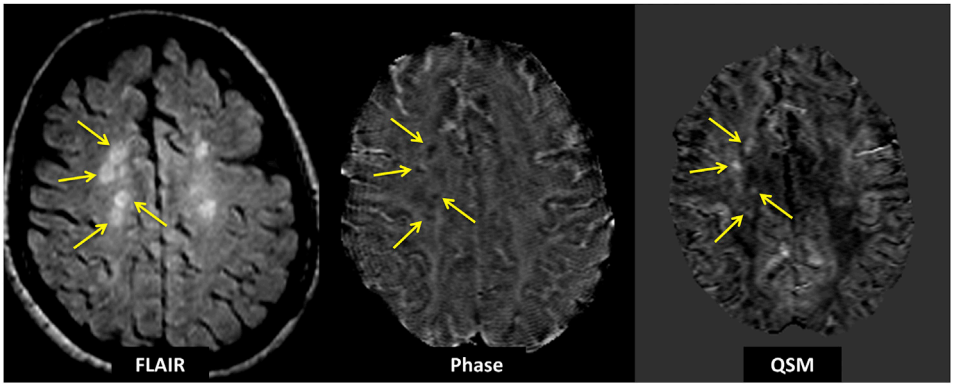

Fig. 3. The FLAIR data (left image) shows numerous white matter MS lesions of which four lesions (noted by yellow arrows) are iron-laden. These lesions appear hypointense on phase (middle image) and hyperintense on QSM (right image). Note that the FLAIR lesions seen on the right side of the image (left side of the brain) do not appear to show changes in susceptibility.

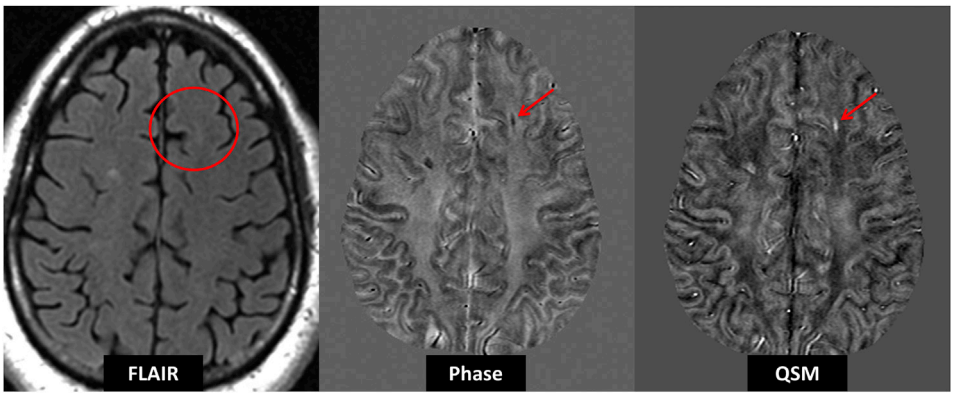

Fig. 4. An example image from an MS subject showing that some lesions can be visualized in phase and QSM that do not appear in FLAIR.

echo or fluid attenuated inversion recovery (FLAIR) images (Polman et al., 2011). During the last decade, SWI and phase imaging have been used to visualize small changes in local susceptibility including, but not limited to, detecting small veins, microbleeds, iron laden macrophages and calcium. Fig. 3 shows an example image of the appearance of MS lesions in FLAIR, phase and QSM. Although there are multiple lesions appearing in the FLAIR image, only four lesions which have iron in them show up in phase and QSM. On the other hand, the first reports of using phase and susceptibility for MS lesions already suggested that up to 35% of the lesions with a change in local susceptibility may not be visible in FLAIR or T2W images (Haacke et al., 2009; Hagemeier et al., 2012). Fig. 4 shows an example image where the lesion does not show in FLAIR, whereas it can be seen in phase and QSM. The question is: "what type of lesions show changes in susceptibility and hence phase?"

One group noted that phase hypointense lesions were significantly more prevalent in patients with active relapsing/remitting MS than with secondary progressive MS (Hagemeier et al., 2012). Another study noted that lesions seen in the phase images at baseline showed no obvious changes in radiological features such as intensity, size, and morphology throughout the course of a 2.5 year follow-up imaging, suggesting that all baseline phase lesions were possibly demyelinated lesions (Bian et al., 2013). According to a recent study, the susceptibilities of early and intermediate MS lesions tend to increase up to roughly 50 ppb higher than normal appearing white matter (NAWM), followed by a gradual reduction back to NAWM over a period of a few years (Chen et al., 2014). This 50 ppb is just at the expected level of susceptibility change in the presence of demyelination (Chen et al., 2014; Li et al., 2016). Other papers using QSM have shown susceptibility changes up to 50 ppb suggesting demyelination while the ring-like structures show higher susceptibility changes suggesting iron in macrophages (Hammond et al., 2008). One paper shows that the high iron seen in the XRF images matches the QSM of a lesion that also had low zinc. This presumably represents demyelinated white matter tissue (Habib et al., 2010). Staining in macrophages and microglia around sites of inflammation shows rims of iron deposits and these correlate with the presence of ferritin (Stephenson et al., 2014). One paper using Perl staining of cadaver brain lesions suggests that there are iron rich M1 macrophages associated with chronic active demyelinating ring-like lesions as seen in the phase images (Mehta et al., 2013). Lesions with myelin have minimal macrophage activity and low intracellular iron (Mehta et al., 2013). Penetrating veins have been shown to appear in about 60% of lesions providing some evidence that MS progresses along veins (Hammond et al., 2008). More specifically, ring lesions are associated with central penetrating veins (Bian et al., 2013).

Phase may offer a better means to see lesions with iron and inflammation since T2* tends to increase with increasing water content and decrease with increasing iron content which may in the end lead to little change in total T2* (Bian et al., 2013; Li et al., 2016). It is also reasonable to assume that phase can be used to visualize changes in myelination. However, using phase contrast alone to examine changes in tissue susceptibility in MS poses some risks (Cronin et al., 2016). The edge effects seen in phase and magnitude images could come from T2* effects in the presence of high gradients at the edge of the lesions (Li et al., 2016). Spatial filtering applied to the phase images is another major factor which affects the exact appearance of lesions. For example, the amplitude of phase variations induced by the lesions was lower in high pass filtered phase images than in the sophisticated harmonic artifact reduction for phase data (SHARP) filtered phase image (Schweser et al., 2011). Also a partial ring structure in high pass filtered phase may not always be a reflection of affected tissue at that point in space but may represent the magnetic field generated by nearby veins (i.e. false positives) (Eskreis-Winkler et al., 2015). Additionally, high pass filtered phase images may

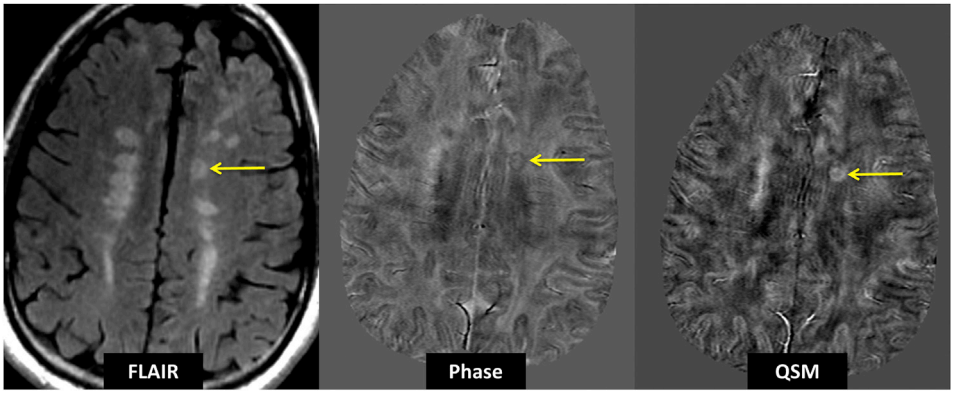

Fig. 5. An example image from an MS subject depicting a ring phase lesion. The hypointense phase rim is clearly visible in the phase (middle) image. However, there seems to be a more uniform distribution of iron in the QSM image. Note that many of the lesions do not exhibit changes in susceptibility.

show edge effects even for otherwise uniformly distributed iron in lesions if the lesions are too big (Cronin et al., 2016). In contrast, QSM provides more accurate information of the geometry of the lesions. Fig. 5 depicts a ring-like lesion where the hypointense ring can be noted in the phase image and a hyperintense ring in the QSM image. Recent studies also showed that QSM can distinguish solid and shell patterns of magnetic susceptibility with greater accuracy than phase imaging, thus suggesting that QSM should be included in future studies on MS lesions (Cronin et al., 2016; Eskreis-Winkler et al., 2015).

It has been shown that combining QSM and R2* can help recognize changes in iron and myelin content during MS lesion development. A study using QSM and R2* demonstrated the myelin breakdown mechanism in early active MS lesions with nodular enhancement where they showed a decrease in R2* but no QSM change (Zhang et al., 2016). They also showed a QSM increase and an R2* decrease in the center of ring lesions showing degradation of myelin debris. Previous studies have shown these changes in R2* and QSM patterns correlate with sequential pathological changes in myelin and iron content that happen during the onset of lesion development (Wang and Liu, 2015; Kutzelnigg and Lassmann, 2014). Another study showed that combining R2* and QSM was useful in better characterizing the susceptibility contrast patterns in MS lesions (Li et al., 2016). To fully address all the combinations possible in interpreting this data, more studies where MS patients are imaged multiple times should be performed to better understand what is happening with the QSM, phase, and R2* identification of MS lesions and how they represent the pathophysiology of MS.

There is some evidence that iron in the caudate nucleus and putamen correlates with the disease (Hagemeier et al., 2012; Hammond et al., 2008; Habib et al., 2012), while more generally MS patients show increases in iron in the midbrain and/or basal ganglia (Habib et al., 2012). Furthermore, Hagemeier et al. found a correlation of T2 and phase with brain atrophy (Hagemeier et al., 2012). However, in terms of correlations with cognitive dysfunction, brain atrophy and physical disability, it has been shown that iron has the best outcomes compared to those of other conventional tissue properties (Stuber et al., 2016). To date, it is unclear if iron is associated with cellular pathology or is simply deposited in the form of ferritin and hemosiderin serving as a biomarker for tissue damage. Using a two-region-of-interest low and high iron content evaluation of the midbrain and basal ganglia, a clear separation between iron content in healthy subjects versus patients with MS was demonstrated in a study of 52 subjects (Habib et al., 2012). The iron weighting factors were abnormal for 13% of healthy subjects and 65% of MS patients, while for patients younger than 40 years, only 1% of healthy subjects and 67% of patients with relapsing/remitting MS showed abnormally high iron content (Habib et al., 2012).

In conclusion, the role of imaging iron in MS continues to evolve with the potential of correlating iron content of the deep gray matter and MS lesions with patient's clinical status and in differentiating demyelinating from inflammatory lesions.

R2 and QSM as a means to measure iron content in Parkinson's disease*

QSM has recently played a major role in research and clinical studies investigating iron deposition in deep gray matter structures of both healthy and diseased conditions (Haacke et al., 2015). One of the most common forms of neurodegeneration is PD which is known to be associated with elevated iron content in deep gray matter and the brain regions responsible for motor function (Wang et al., 2016; Martin-Bastida et al., 2017). Although other advanced post-processing MR techniques such as phase, R2 and R2* maps have been utilized to quantify iron content, QSM has proven to be a more promising and reliable method in terms of sensitivity and specificity (Barbosa et al., 2015; Haacke et al., 2015; Du et al., 2016; Murakami et al., 2015; Langkammer et al., 2016). Iron deposition has been found to be inhomogeneously distributed in the brains of PD patients (Wang et al., 2012; Dashtipour et al., 2015). However, the most prominent deficit is the degeneration of dopaminergic interactions in the substantia nigra (SN) which leads to high levels of non-heme iron in this midbrain structure (Ayton and Lei, 2014; Gorell et al., 1995). Cross-sectional and longitudinal research studies have quantitatively investigated this abnormality by monitoring the patients' iron-rich brain structures, particularly in the SN. In this section, we only focus on R2* and QSM techniques which are the most widely used iron quantification methods in PD.

Using R2* maps, several studies have found abnormally elevated R2* rates, putatively indicative of higher iron deposition, across different subcortical brain regions in PD patients either in comparison with healthy control groups or after a specific period of time when monitored longitudinally. In the form of a cross-sectional study, Gorell et al. demonstrated higher R2* values in the SN of a non-demented PD group compared to a healthy cohort (Gorell et al., 1995). Rossi et al. showed increased levels of R2* not only in the SN, but also in the globus pallidus compared to a normal group (Rossi et al., 2013). In another article, however, Hopes et al. claimed that nigrostriatal structures including the SN, caudate nucleus and putamen had significantly greater R2* values in untreated PD patients compared to a healthy cohort (Hopes et al., 2016). Esterhammer et al. demonstrated a significant increase of R2* in the putamen and globus pallidus only in the early stages of PD with the SN maintained significant in both early and advanced stages (Esterhammer et al., 2015). On the other hand, two longitudinal R2* studies by Ulla et al. and Wieler et al. have both reported an increase in the R2* rate of SN over a 3-year time period indicating that the iron content in the PD patients progresses over time (Ulla et al., 2013; Wieler et al., 2015). Ulla et al. also reported a significant progression of iron deposition in the caudal putamen (Ulla et al., 2013).

Over the past decade, QSM has been used to investigate iron related pathology and progression of PD. Similar to R2*, QSM has also shown higher levels of iron accumulation in the brains of PD patients, particularly in the SN (Barbosa et al., 2015; Du et al., 2016; Murakami et al., 2015; Langkammer et al., 2016). Guan et al. showed that susceptibility values are directly correlated with the disease stage and claimed that substantia nigra pars compacta (SNpc) is characterized by significantly higher iron content only in the early stages, whereas in more advanced stages of PD other structures such as substantia nigra pars reticulata (SNpr), red nucleus and globus pallidus also tend to develop high levels of iron deposition (Guan et al., 2017a). Elevated iron content in the SNpc was also reported in a 7 T high resolution QSM study done by Lotfipour et al. in which significantly higher magnetic susceptibility values were seen for this substructure in the PD patients compared to a control group (Lotfipour et al., 2012). In Azuma et al.'s work, QSM was found to be a useful technique for quantitatively assessing lateral asymmetries in the SN of PD patients where the hemisphere differences were more prominent compared to those of the healthy controls (Azuma et al., 2016). Another study by Guan et al. showed that depending on the type of PD, the structures characterized by high iron accumulation vary. They claimed that iron accumulation in the nigral regions is the dominant effect in PD regardless of the disease type, whereas excessive iron deposition in the DN and red nucleus was seen only in patients with tremor symptoms (Guan et al., 2017b). Similarly, in a study done by He et al. the DN was shown to be the structure of choice that could be a potential biomarker to differentiate tremor-dominant PD from other types due to the increased magnetic susceptibility values only in this cerebellar structure (He et al., 2017). Conversely, Acosta-Cabronero et al. reported that although magnetic susceptibility is expectedly higher in the dorsal SN, iron content in the DN decreases in idiopathic PD compared to healthy controls (Acosta-Cabronero et al., 2017).

To date, the high iron content of the SN appears to serve as the only reliable biomarker to characterize PD as has been consistently reported in the literature (Barbosa et al., 2015; Du et al., 2011, 2016; Wang et al., 2016; Murakami et al., 2015; Langkammer et al., 2016; Gorell et al., 1995; Rossi et al., 2013; Hopes et al., 2016; Esterhammer et al., 2015; Ulla et al., 2013; Wieler et al., 2015; Guan et al., 2017a; Lotfipour et al., 2012; Azuma et al., 2016; Acosta-Cabronero et al., 2017; Peran et al.,

2010; He et al., 2015). Moreover, in a few studies where both R2* and QSM techniques were used to quantify iron content in PD patients, QSM showed superior sensitivity and accuracy in terms of diagnostic performance as well as detecting significant differences between PD and healthy groups making it the preferred in vivo iron quantification technique (Barbosa et al., 2015; Du et al., 2016; Murakami et al., 2015; Langkammer et al., 2016). This could be due in part to the fact that increased water content can confound increases in iron content making R2* less sensitive. On the other hand, increased water content does not affect the susceptibility from the local iron deposition making QSM potentially more valuable in the assessment and quantification of iron content.

Under normal conditions, non-heme iron levels also change in the aging brain. Assessing quantified iron content against normal aging across brain structures dates back to the 1950s when Hallgren and Sourander investigated iron concentration in cadaver brains (Hallgren and Sourander, 1958). Over the past few decades, several research groups have tried to quantify normal brain iron content versus age with in vivo MR post-processing techniques. By using QSM, Li et al. introduced baselines of magnetic susceptibility changes as a function of age over the lifespan in cortical and subcortical brain regions (Li et al., 2014a). In addition to validating their normal susceptibility-age baselines through a 3D ROI-based algorithm (known as the global analysis) for different deep gray matter nuclei, Liu et al. developed a new algorithm by which the local high iron content can be detected depending on the structure of interest and the age of the subject (Liu et al., 2016a). In this algorithm, the upper 95% prediction interval from the susceptibility-age global analysis of each nucleus is used to define an age-dependent threshold. Any voxel within the associated 3D ROI with a susceptibility value higher than that threshold would be considered as a high iron content (RII) voxel. The mean RII susceptibilities as a function of age for different deep gray matter structures then establish new normal baselines, known as the regional analysis, which is claimed to have higher sensitivity, reliability and robustness for monitoring age-dependent changes in iron content compared to the global analysis (Liu et al., 2016a).

Fig. 6 shows the global and regional mean susceptibility values against age in the SN for a population of 174 healthy controls used in Liu et al.'s study serving as a baseline for 22 idiopathic Parkinson's disease (IPD) patients (Liu et al., 2016a). These 22 patients were scanned on a 3.0 T Skyra MR system (Siemens, Germany) with a twenty-channel head/neck coil. The 3D SWI imaging parameters were: TE/TR = 20/30 ms, flip angle = 15°, slice thickness = 2 mm, pixel bandwidth = 120 Hz/pixel and an in-plane resolution of $0.5 \times 0.5\ mm^2$. The analysis of covariance (ANCOVA) revealed that the rate of mean susceptibility change as a function of age (i.e. the linear regression slope), determined by the regional analysis, was significantly different from that of the healthy population in the SN (p-values = 0.02 for both the right and left SN). On the other hand, the global analysis did not reveal any significant difference in the slope for the PD patients compared to the healthy controls. What aspects of the disease this correlates with remains to be determined.

Table 2 reviews the studies investigating the brain iron content in cohorts of PD patients compared to healthy controls using R2* and QSM techniques. As shown in the table, the SN is the only deep gray matter nucleus which is consistently showing significantly elevated iron deposition in PD patients compared to healthy controls across all the reported studies (Barbosa et al., 2015; Du et al., 2011, 2016; Murakami et al., 2015; Langkammer et al., 2016; Rossi et al., 2013; Hopes et al., 2016; Esterhammer et al., 2015; Ulla et al., 2013; Wieler et al., 2015; Guan et al., 2017a, 2017b; Lotfipour et al., 2012; Azuma et al., 2016; Peran et al., 2010; He et al., 2015; Ji et al., 2016; Acosta-Cabronero et al., 2017). Furthermore, in a few studies this significance expands to substructures of the SN, particularly the SNpc (Barbosa et al., 2015; Du et al., 2016; Rossi et al., 2013; Ulla et al., 2013; Wieler et al., 2015; Guan et al.,

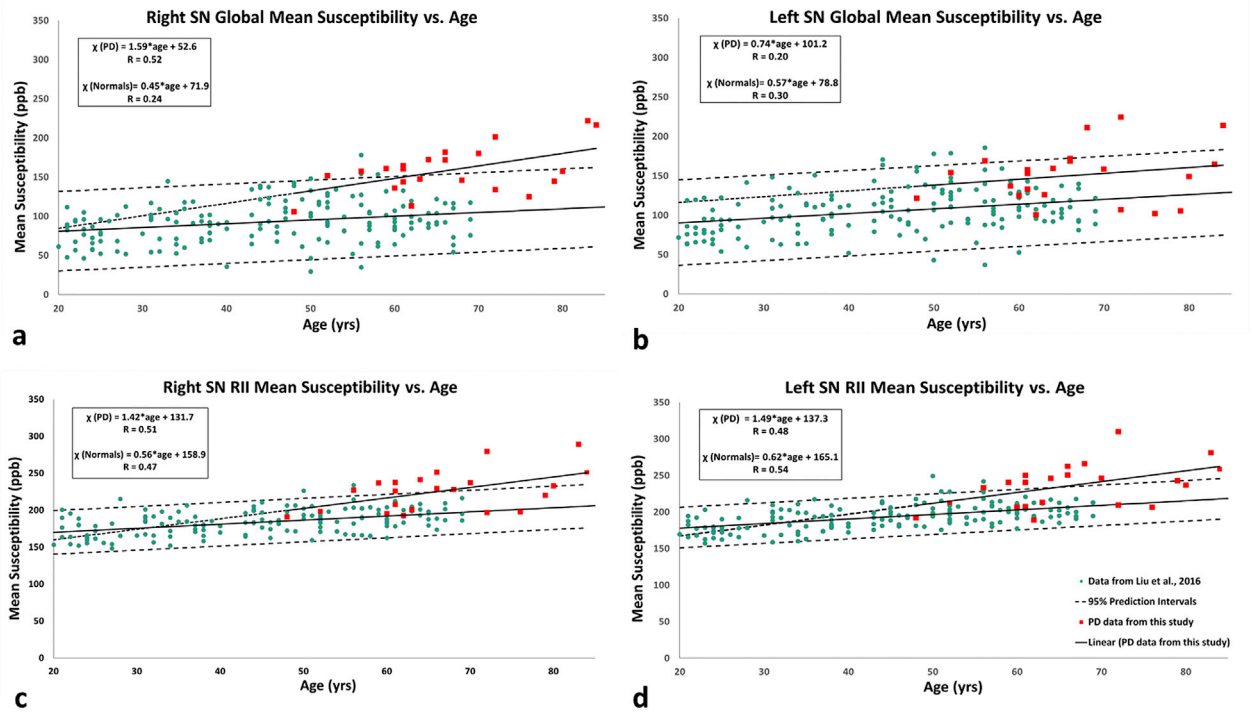

Fig. 6. Magnetic susceptibility of the substantia nigra measured in 22 IPD patients compared to the normal baseline provided by Liu et al. (2016a) a,b) global (entire structure) analysis of the PD patients compared to Liu et al.'s study. c,d) regional (high iron content) analysis of the PD patients compared to Liu et al.'s study. Blue circles: data from Liu et al., dashed lines: 95% prediction intervals from the normal population, solid lines: linear regression model, red squares: PD patients. Equations and the Pearson correlation coefficients belong to the linear regression models. The slopes of the linear regression model for the PD patients were found to be significantly different than those of the normal controls in the regional analysis (c and d), but not in the global analysis (a and b).

2017a, 2017b; Lotfipour et al., 2012; Azuma et al., 2016; Acosta-Cabronero et al., 2017). By taking the mean of the increased rates in the SN and SNpc in the studies in which statistical information are provided (see Table 2), the average increased rates were 10.3 ± 8.5% and 13.6 ± 4.0% in the R2* values of the SN and SNpc, respectively, in the PD patients compared to the healthy controls. However, these changes are reflected in considerably higher rates when QSM techniques were used. Specifically, the average increase rates were 28.2 ± 14.6% and 35.2 ± 2.7% for the SN and SNpc, respectively. These increased rates in R2* and QSM reflect elevated levels of iron concentration in these structures. However, these may be an under-estimation of the actual changes of the iron content in the SN, since the voxels with low levels of iron content were included in those studies and because all PD patients were included not just those showing high iron content in the SN. As shown in Fig. 6, much higher susceptibilities of the SN were observed when a regional analysis was used (Fig. 6c–d).

Iron-age baseline in the dentate nucleus

In addition to the SN being characterized by high levels of iron deposition in PD patients, a few recent studies have investigated magnetic susceptibility values in the DN of PD patients as compared to matched healthy groups (Guan et al., 2017b; He et al., 2017; Acosta--Cabronero et al., 2017). However, both Guan et al. and He et al. have demonstrated increased susceptibility values in the DN of tremor-dominant PD patients (Guan et al., 2017b; He et al., 2017), while another QSM study by Acosta-Cabronero et al. showed reduced iron content in the DN of IPD patients (Acosta-Cabronero et al., 2017). The variations reported in these studies and the fact that evaluating iron changes in the DN through QSM appears to be a fairly new realm necessitates establishing a reliable normal susceptibility-age baseline of this structure to which data from PD patients could be compared. Furthermore, magnetic susceptibility changes in the DN is important to study since it has been recently implicated that gadolinium (Gd), a paramagnetic metal which acts like iron, tends to accumulate in the DN after multiple administrations of gadolinium-based contrast agents (GBCA) (Kanda et al., 2014, 2016; Stojanov et al., 2016; Tedeschi et al., 2016). This too necessitates the need for a normal baseline from which elevated levels of paramagnetism under abnormal conditions can be quantitatively monitored.

In order to establish an in vivo DN susceptibility baseline as a function of age, eighty-one healthy subjects (39.14 ± 12.56, age range 20–61 years old) were scanned with a 3D gradient recalled echo (GRE) sequence using a 3.0 T TRIO scanner (Siemens, Erlangen, Germany) with the following imaging parameters: TR/TE = 20/29 ms, FA = 15°, slice thickness = 2 mm, bandwidth/pixel = 120 Hz/pxl and matrix size (Nx × Ny) = 448 × 336 resulting in an in-plane resolution of 0.5 × 0.5 mm^2. The method of QSM reconstruction, the 3D manual ROI drawing criteria and both global and regional analyses were identical to those of Liu et al.'s study (Liu et al., 2016a). Fig. 7 shows the mean susceptibility values extracted from the entire structure and the high iron content region. To validate the global analysis approach, the results were compared to another QSM study by Li et al. within a similar age range (Li et al., 2014a). The linear regression models were also applied to evaluate the correlation between susceptibility and age in both analyses. In addition to the DN global analysis showing a very good agreement with Li et al.'s work (Li et al., 2014a), the higher slope, the narrower 95% prediction interval and the higher Pearson correlation coefficient (PCC) values in the regional analysis confirms greater sensitivity and precision of this technique in the DN as well, similar to other deep gray matter nuclei addressed in Liu et al.'s study (Liu et al., 2016a). Based on these results, the RII approach may prove to be a more sensitive and robust baseline in studying abnormally high levels of iron content in neurodegenerative diseases and gadolinium deposition in patients undergoing multiple contrast agent administrations.

T2 and T2′ as a means to measure iron tagged cells*

MRI offers the potential to image iron tagged cells and small amounts of iron with high susceptibility (Kokeny et al., 2017). The only question in terms of measuring the number of cells that have been tagged is the SNR. In order to detect the presence of signal over background noise, the contrast-to-noise ratio (CNR) should be at least 4:1 according to the Rose criteria. Iron tagging is an efficient means to enhance signal loss and increase contrast since iron tagged cells can create an effective volume loss on the order of one million times the size of the object. The use of USPIO fits the bill to accomplish this signal loss enhancement.

Iron oxide particles are the most often used reagents to label cells. With different coating methods, a variety of iron oxides particles have been developed (Shen et al., 2016; Leder et al., 2015; Shahnaz et al., 2013; Li et al., 2013; Vetter et al., 2011; Lee et al., 2011a). For efficient labeling, these iron oxide particles must have obvious influence on relaxation rates without affecting cell proliferation (Thu et al., 2012; Long et al., 2015). R2* methods are better to use because they are more sensitive to changes in iron content than R2 and the fact that the data can be rapidly collected in 3D (Runge et al., 2016; Wang et al., 2014). Signal loss from R2* effects has been shown to be linearly correlated with labeling concentration (Kasten et al., 2014). Bowen et al. found that the R2* relaxation rate for iron oxide loaded cells was 70 times higher than for R2 using a 2D hybrid relaxometry pulse sequence at 1.89 T and a 2D multi-echo Carr-Purcell-Meiboom-Gill (CPMG) imaging pulse sequence at 4 T (Bowen et al., 2002). Others have studied the use of R2′ as a means to increase sensitivity in depicting subtle changes in iron content (Ruggiero et al., 2013). Shichinohe et al. suggested that at least 1000 bone marrow stromal cells (BMSC) labeled with superparamagnetic iron oxide (SPIO) could be tracked by T2*-weighted images at 3 T (Shichinohe et al., 2012). Another study showed that MRI was able to detect 1000 ferumoxytol-heparin-protamine (HPF) nanocomplex labeled cells implanted in rat brains also by T2*-weighted images (Thu et al., 2012). Vernikouskaya et al. labeled mesenchymal stromal cells (MSCs) with iron oxide loaded poly-(l-lactide) (iPLLA) nanoparticles and got an average cellular iron content of 55 pg iron per cell (Vernikouskaya et al., 2014). These iPLLA nanoparticles' high R2* relaxivity (545 $mM^{-1}s^{-1}$) enabled the visualization of a single labeled cell in vitro with 50 μm spatial resolution. This paper nicely demonstrates the role of resolution as it affects concentration per voxel. For example, increasing the voxel size to 250 μm isotropically requires 125 times more cells, or in this case 125 cells to still see an effect on the signal. They used an echo time of 2.8 ms at 11.7 T which is equivalent to an echo time of roughly 11 ms at 3 T. Further improvements in detection can be obtained by increasing the echo time. One can approximate the number of cells that would be required to be visible as a function of the voxel size, R2* ($mM^{-1}s^{-1}$), TE (in ms), B_o (in T) and voxel volume V_{voxel} (in mm (St Pierre et al., 2005)) as follows:

$$N_{cells} = \left(\frac{545}{R2^*}\right)\left(\frac{2.8}{TE}\right)\left(\frac{11.7}{B_o}\right)(8000V_{voxel}). \quad (10)$$

Iron-labeled stem cells remain an important area of research since they are able to target tumors and provide potential therapies (Gutova et al., 2013; Pereira et al., 2015; Campan et al., 2011; Deans et al., 2006; Kedziorek and Kraitchman, 2010; Thu et al., 2009; Cheung et al., 2006; Tang et al., 2011). Mishra et al. found an 8-fold increase in R2 in Fe-Pro complex labeled MSCs compared with unlabeled cells using a relaxometry study (Mishra et al., 2017). Monitoring of iron-labeled MSCs by MRI enabled investigations on the migration of MSCs in the brain (Reddy et al., 2010; Granot et al., 2013), and explorations on stem cell therapies for bladder outlet obstruction (BOO) (Lee et al., 2012a). Besides MSCs, many other types of stem cells have been studied. Iron-labeled neural stem cells (NSCs) were visible up to 10 days in C6 glioma bearing nude mice post injection by T2*-weighted images (Kim et al., 2016). Ferumoxides and protamine sulfate complex labeled embryonic stem cell-derived cardiac-precursor-cells (ES-CPCs) have been imaged in vivo

Table 2
Recent studies on R2* and QSM comparing different brain structures in PD patients and healthy controls.

Study	Sample Size (N)	Iron Quantification Method	Field Strength	Brain Structures Assessed	Brain Structures with Significant Differences in PD vs. HC	(Mean ± SD in HC, Mean ± SD in PD)[a]
Peran et al. (2010)	22 HC, 30 PD	R2*	3 T	CN, GP, PUT, THA, RN, SN	SN	NA
Du et al. (2011)	16 HC, 16 PD	R2*	3 T	SN	SN	NA
Rossi et al. (2013)	21 HC, 34 PD	R2*	3 T	SN, GP	Medial SNpc, Lateral SNpc	Medial SNpc: (43 ± 7, 51 ± 10) Lateral SNpc: (42 ± 6, 50 ± 10)
[b] Ulla et al. (2013)	26 HC (8 M, 18 F), 27 PD (13 M, 14 F)	R2*	1.5 T	GP, PUT, SN, GM, WM	SNpc, SNpr	SNpc-M: (20.2 ± 0.41, 22.7 ± 0.48) SNpc-F: (20.9 ± 0.39, 22.5 ± 0.61) SNpr-M: (25.3 ± 1.10, 28.7 ± 0.95) SNpr-F: (25.1 ± 0.4, 25.5 ± 0.50)
[c] Ulla et al. (2013)	18 HC, 14 PD	ΔR2*	1.5 T	GP, PUT, SN, GM, WM	SNpc, SNpr, PUT	NA
Wieler et al. (2015)	13 HC, 19 ES-PD	R2*	3 T	GP, PUT, RN, SN	SNpc	NA
Murakami et al. (2015)	21 HC, 21 PD	R2*	3 T	CN, GP, PUT, THA, RN, SN	SN	SN: (29.0 ± 2.0, 30.1 ± 1.5)
Esterhammer et al. (2015)	38 HC, 82 PD	R2*	1.5 T	CN, GP, PUT, THA, SN, CC	SN	SN: (20.58 [17.4–23.9], 21.25 [15.8–29.4])[d]
He et al. (2015)	35 HC, 44 ES-PD	R2*	3 T	CN, GP, PUT, RN, SN	SN	SN: (34.9 ± 4.41, 38.9 ± 5.91)
Barbosa et al. (2015)	30 HC, 20 PD	R2*	3 T	CN, GP, PUT, THA, RN, SN	SNpc	SNpc: (47.7 ± 8.4, 52.8 ± 11.7)
Du et al. (2016)	47 HC, 47 PD	R2*	3 T	SN	SNpc	SNpc: (32.8 ± 5.0, 37.8 ± 4.3)
Hopes et al. (2016)	20 HC, 15 LS-PD	R2*	3 T	CN, GP, PUT, SN	L-SN, R-SN	L-SN: (37.7 [36–39], 50.2 [45–52])[d] R-SN: (36.8 [35–39], 47.8 [45–52])[d]
Ji et al. (2016)	28 HC, 54 PD	R2*	3 T	CN, GP, PUT, THA, RN, SN	L-SN, R-SN, L-RN, R-RN	L-SN: (34.2 ± 0.85, 37.0 ± 0.74) R-SN: (34.6 ± 0.97, 37.3 ± 0.69) L-RN: (29.7 ± 0.61, 31.7 ± 0.64) R-RN: (29.3 ± 0.68, 31.7 ± 0.54)
Langkammer et al. (2016)	58 HC, 66 PD	R2*	3 T	CN, GP, PUT, THA, RN, SN	SN	SN: (37.6 ± 5.8, 41.1 ± 8.7)
Guan et al. (2017a)	40 HC, 45 ES-PD, 15 LS-PD	R2*	3 T	CN, GP, PUT, THA, RN,SN, DN	SNpc	NA
Guan et al. (2017b)	40 HC, 27 TD-PD, 27 AR-PD	R2*	3 T	CN, GP, PUT, THA, RN,SN, DN	SNpc	NA
Lotfipour et al. (2012)	11 HC, 6 TD-PD, 3 PIGD	QSM	7 T	SN	SNpc	NA
Murakami et al. (2015)	21 HC, 21 PD	QSM	3 T	CN, GP, PUT, THA, RN, SN	SN	SN: (199.0 ± 14.0, 224.0 ± 14.0)
He et al. (2015)	35 HC, 44 ES-PD	QSM	3 T	CN, GP, PUT, RN, SN	SN, RN	SN: (83.7 ± 15.6, 100.0 ± 18.3) RN: (81.0 ± 14.5, 93.0 ± 18.9)
Barbosa et al. (2015)	30 HC, 20 PD	QSM	3 T	CN, GP, PUT, THA, RN, SN	SN, SNpc	SN: (114.7 ± 32.5, 150.9 ± 41.5) SNpc: (140.1 ± 38.5, 186.7 ± 53.2)
Du et al. (2016)	47 HC, 47 PD	QSM	3 T	SN	SNpc	SNpc: (108.0 ± 33.0, 148.0 ± 44.0)
Acosta-Cabronero et al. (2017)	50 HC, 25 PD	QSM	3 T	Whole-brain pattern, SN	SN, vSN, dSN, LOC, PPC, RMPC, MTC, DN, HIP	NA
[e] Azuma et al. (2016)	25 HC, 24 PD	QSM	3 T	CN, GP, PUT, RN, SN	SN, mSN, pSN	SN: (104.7 ± 31.0, 158.0 ± 47.6) mSN: (104.6 ± 28.7, 166.6 ± 53.2) pSN: (66.5 ± 25.6, 120.8 ± 38.7)
Langkammer et al. (2016)	58 HC, 66 PD	QSM	3 T	CN, GP, PUT, THA, RN, SN	SN, RN, GP, THA	SN: (90.0 ± 30.0, 114.0 ± 40.0) RN: (89.0 ± 30.0, 105.0 ± 40.0) GP: (112.0 ± 30.0, 126.0 ± 30.0) THA: (0.0 ± 10.0, 5.0 ± 10.0)
Guan et al. (2017a)	40 HC, 45 ES-PD	QSM	3 T	CN, GP, PUT, THA, RN,SN, DN	SNpc	NA
Guan et al. (2017a)	40 HC, 15 LS-PD	QSM	3 T	CN, GP, PUT, THA, RN,SN, DN	SNpc, SNpr, RN, GP	NA
Guan et al. (2017b)	40 HC, 27 TD-PD	QSM	3 T	CN, GP, PUT, THA, RN,SN, DN	SNpc, RN, DN	NA
Guan et al. (2017b)	40 HC, 27 AR-PD	QSM	3 T	CN, GP, PUT, THA, RN,SN, DN	SNpc	NA
He et al. (2017)	48 HC, 19 TD-PD	QSM	3 T	DN	DN	DN: (63.0 ± 16.0, 74.0 ± 18.0)

Abbreviations: M: male, F: female, L: left, R: right, HC: healthy control, PD: Parkinson's disease, SN: substantia nigra, TD-PD: tremor dominant PD, AR-PD: akinetic-rigid dominant PD, PIGD: postural instability gait disorder, LS-PD: late stage PD, ES-PD: early stage PD, SNpc: SN pars compacta, SNpr: SN pars reticulata, mSN: middle part of the SN, pSN: posterior part of the SN, vSN: ventral SN, dSN: dorsal SN, PUT: putamen, DN: dentate nucleus, RN: red nucleus, THA: thalamus, GP: globus pallidus, GM: gray matter, WM: white matter, HIP: hippocampus, LOC: lateral occipital cortex, PPC: posterior parietal cortex, MTC: middle temporal cortex, RMPC: rostral middle prefrontal cortex. CC: corpus callosum, NA: not available.

[a] Units of R2* and QSM are in s^{-1} and ppb, respectively.

[b] In this study, by combining male and female groups, an analysis of variance (ANOVA) showed a significant increase of R2* in PD compared to HC group in both SNpr and SNpc.

[c] ΔR2* corresponds to the difference in the R2* value between the baseline and a follow up time-point after 3 years.
[d] In this study, R2* values are quoted as median [range].
[e] In this study, QSM values for the PD patients were quoted from the more affected hemibrain.

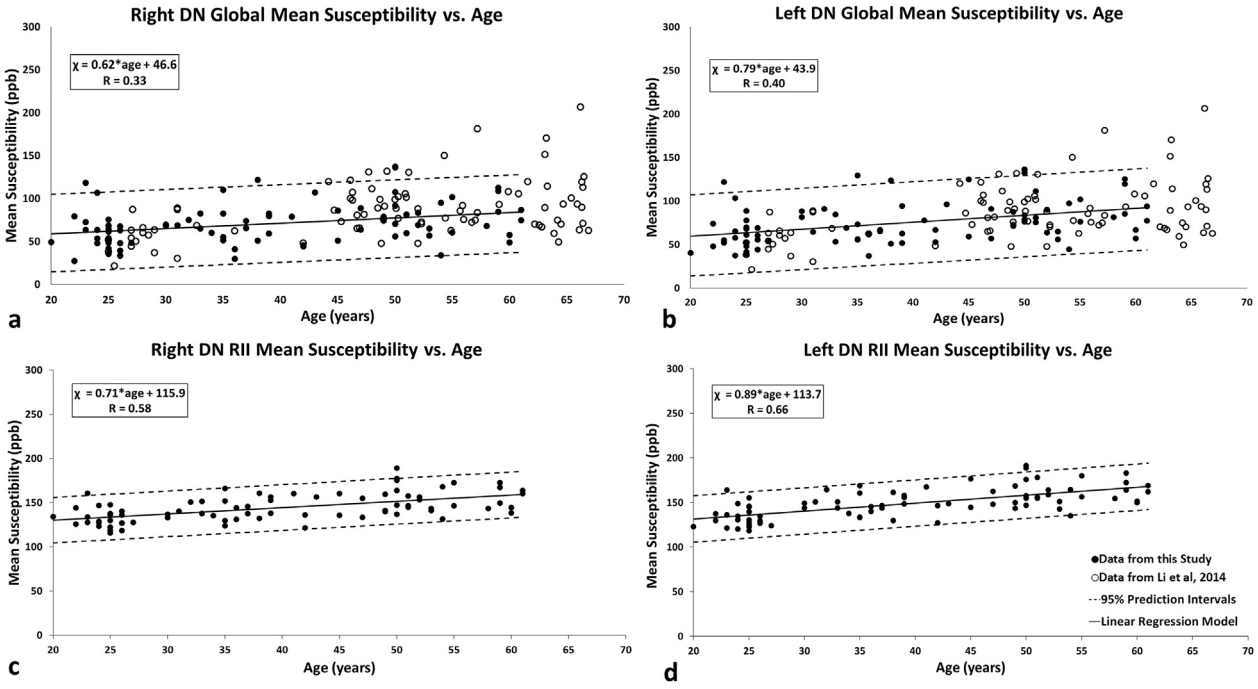

Fig. 7. Susceptibility changes of the dentate nucleus as a function of age in both hemispheres. a,b) global (entire structure) analysis of the DN compared to Li et al.'s study within a similar age range (Li et al., 2014a). c,d) regional (high iron content) analysis of the DN. The results of the global analysis are consistent with Li et al.'s study. Open black circles: data from Li et al., filled black circles: data from this study, black solid lines: linear regression models fitted to the data. Dashed lines: 95% prediction intervals applied to the data from this study. Equations belong to linear regression model and the information in the inserts include the Pearson correlation coefficients.

using a T2* weighted sequence (negative contrast) and a positive contrast gradient acquisition for superparamagnetic particles/susceptibility (GRASP) technique (Mani et al., 2008). There are controversies about the fate of stem cells post injection. Some studies showed that NSCs were self-eliminated during the course of anti-cancer therapy (Aboody et al., 2006a, 2006b; Danks et al., 2007). However, cell division was observed in Fe-Pro-labeled NSCs (Thu et al., 2009), overthrowing the idea that NSCs do not divide in vivo. Living cells were supposed to be distinguished from dead cells with different R2 relativities, as demonstrated in one study that discriminated live iron-labeled cells and lysed iron-labeled cells in vitro and in vivo using a b-SSFP sequence (Ribot and Foster, 2012), but no difference in the appearance on T2 weighted images was observed between living and dead cells (Ruggiero et al., 2013). The discrepancy may be caused by different parameters and pulse sequences applied in each study. A major concern of tracking iron-labeled cells is the gradual MRI signal loss after injection (Thu et al., 2009; Gaudet et al., 2016; Economopoulos et al., 2013). One explanation is that dead cells may transfer iron oxides into macrophages, since iron-loaded macrophages were seen (Higuchi et al., 2009). The study of Noad et al. further proved this idea, in which MRI signal loss was slower in severely immune-compromised mice than in immune-competent mice (Noad et al., 2013). Another explanation is that migration of cells may account for this (Vreys et al., 2011), which is also confirmed by histological studies (Reddy et al., 2010). Other studies showed that iron nanoparticles will enter the normal iron metabolic pathways and may potentially disappear from sight in the MR images because they are no longer magnetic (Arbab et al., 2005; Pawelczyk et al., 2006; Toso et al., 2008).

Another exciting direction is the creation of various MRI reporter genes to provide a window for in vivo visualization of physiologic processes (Vandsburger et al., 2013; Vande Velde et al., 2013; Li et al., 2011). Ferritin is one of the most popular reporter genes because of its stability both in vivo and in vitro and its capability of holding thousands of iron atoms (Arosio and Levi, 2002; Aisen et al., 2001). Fluorescence imaging can be combined with MRI by making dual-reporter genes that express both fluorescent proteins and ferritins, such as myc-tagged human ferritin heavy chain (myc-hFTH) and green fluorescent protein (GFP) co-expression in human tumor cells MCF-7 (Kim et al., 2010), heavy chain ferritin and DsRed fusion protein (ferritin-DsRed) in GL261 mouse glioma cells (Ono et al., 2009). However, long-term expression of ferritin could lead to potential harm to the body (Hasegawa et al., 2012; Guo et al., 1998; Friedman et al., 2011). This concern was later alleviated controlling for ferritin expression by turning it on with the addition of tetracycline (Wilkinson et al., 2006; Feng et al., 2012; Cohen et al., 2005, 2007). In a recent work, a novel tetracycline-regulated ferritin–EGFP chimera was expressed in human glioma U251 cells which was able to cause an obvious MRI contrast effect without affecting cell proliferation (Jiang et al., 2017).

In summary, MRI offers the means to measure the presence of and monitor the changes to cells and proteins that are tagged with iron. This makes MRI not only a valuable tool for basic studies of the properties of tagged materials but also for future in vivo use as well.

Measuring iron content in blood vessels in the presence of USPIO contrast agents

In addition to the quantification of endogenous iron content, the quantification of exogenous iron content, particularly iron oxide nanoparticles (IONP) based contrast agents, also has many important applications, such as estimating the cerebral blood volume (CBV), imaging the microvasculature and tracking iron labeled stem cells (Kim et al., 2013;

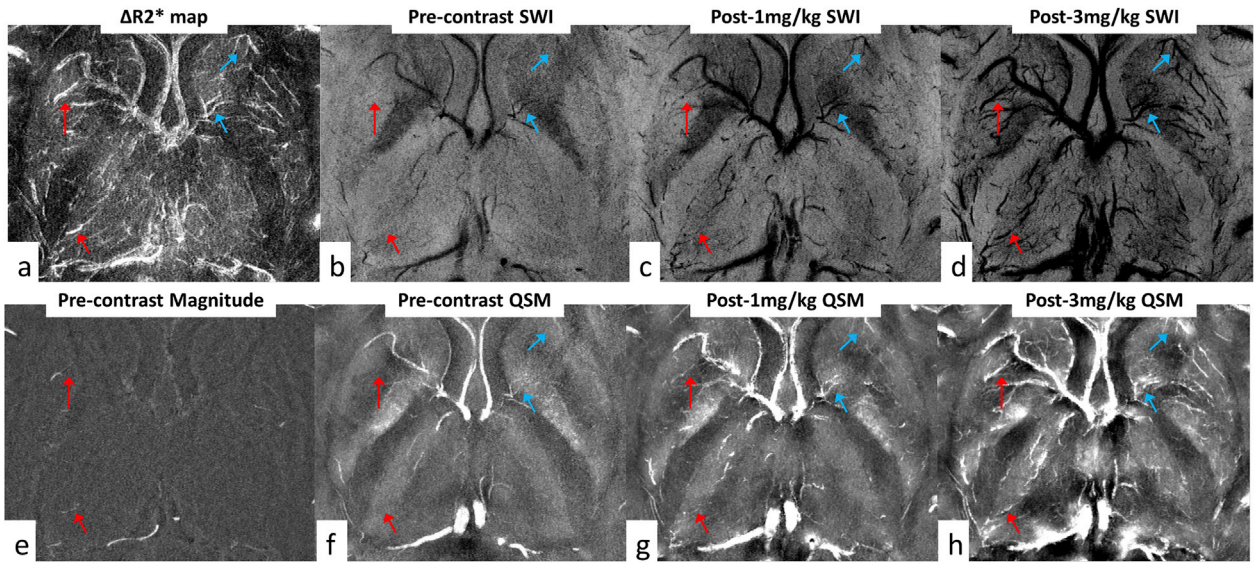

Fig. 8. Visualization and quantification of cerebral arteries and veins using a ΔR2* map (a), SWI (b to d) and QSM (f to h) with ferumoxytol at 7 T. With ferumoxytol, small arteries (red arrows) and veins (blue arrows) which may not be visible in the pre-contrast magnitude image (e) can now be visualized and quantified. b, c and d are minimum intensity projections, while the other images are all maximum intensity projections. The ΔR2* map (a) was generated using the pre- and post-contrast magnitude images. The pre-contrast magnitude image shown in (e) was high-pass filtered for better visualization of the vessels. The effective slice thickness is 3.2 mm for all the images.

Bull et al., 2014; Han et al., 2015; Liu et al., 2017b). Typically, the quantification of IONP concentration is achieved by measuring the changes in the R1, R2, or R2* relaxation rates, using either GRE or ultrashort echo (UTE) sequences (Kim et al., 2013; Han et al., 2015; Girard et al., 2012; Gharagouzloo et al., 2015; Hong et al., 2017). It has been shown that UTE sequences are more advantageous than GRE sequences for quantifying high concentration of IONP, such as those used for IONP based hyperthermia (Han et al., 2015; Hong et al., 2017; Zhang et al., 2014). As demonstrated by Zhang et al. by using a UTE sequence with R1 mapping, IONP with concentrations up to 53.6 mM can be reliably quantified (Zhang et al., 2014). Since the R2* relaxation rate can be influenced by the field inhomogeneity and the orientation dependence of field variation, the accuracy of IONP concentration quantification through R2* mapping may be compromised, while R1 mapping with the UTE sequence provides more reliable results (Han et al., 2015). When compared with the CBV estimation using R1 mapping with the UTE sequence, the R2* mapping based CBV measurement showed more variation, mainly due to the orientation dependence of R2* and the sensitivity of R2* to field inhomogeneities (Han et al., 2015).

Although both the accuracy and precision of IONP quantification can be improved by optimizing the imaging parameters (Gharagouzloo et al., 2015), the accuracy of these relaxation mapping based methods is limited, since the R2 and R2* relaxation rates are dependent on the size of the particles and the diffusion related contrast mechanism (Yablonskiy and Haacke, 1994; Girard et al., 2012). As shown by Girard et al. R2 and R2* mapping based iron quantification may not be reliable for quantifying mixtures of free and internalized IONPs. On the other hand, the magnetic susceptibility provides a more robust means for quantifying IONP concentrations, regardless of the state of the particles (Girard et al., 2012). Additionally, due to the magnetization saturation effect, the effective susceptibility of ferumoxytol, a type of USPIO, with certain concentration will be proportionally higher at a lower field strength, compensating for the loss of SNR at a lower field strength (Liu et al., 2017b). Hence, QSM based methods have great potential for quantifying IONP concentration. There are also benefits in quantifying the IONP concentration using a multiparametric approach. By quantifying R1, R2, R2* and susceptibility of the IONP, it becomes viable to study the microvasculature properties, such as cerebral blood volume, mean vessel size, or angiogenesis (Kim et al., 2013; Han et al., 2015; Girard et al., 2012; Gambarota et al., 2006). Moreover, by utilizing the susceptibility effects of ferumoxytol small arteries and veins can be visualized and quantified (Liu et al., 2017b), as demonstrated in Fig. 8. This provides an important tool for studying neurovascular diseases with microvascular origins. Ferumoxytol is an FDA approved drug for treating iron-deficient anemia; there have been many studies using ferumoxytol as an off-label contrast agent (Liu et al., 2017b; Vasanawala et al., 2016; Finn et al., 2017). Although the typical dose of ferumoxytol is much lower when used as a contrast agent, care should be taken when it is administered in vivo (FDA Drug Safety Communication, 2015).

Recommendations and conclusions

Although the choice of the optimal method depends heavily on the purpose of the study, in this section we provide a discussion on the iron quantification methods and give recommendations for a few popular research topics for which iron quantification is needed. First, for quantifying cerebral iron content, the combination of R2* and QSM is recommended. It has been shown that R2* is more sensitive to the changes of cerebral iron content than R2, and QSM has even superior sensitivity than R2* (Langkammer et al., 2010, 2013; Walsh et al., 2013). Compared with R2*, QSM shows better reproducibility due to its independence of main field strength and imaging parameters. The reproducibility of QSM can be reflected by the consistent slopes in the relationships between susceptibility and iron concentration found in different studies conducted at different field strength, whereas the slopes found in studies using R2* showed a clear dependence on the main field strength, as shown in Table 1. This makes QSM a better choice in longitudinal studies or studies comparing results obtained from other imaging sites using different data acquisition protocols. Nonetheless, studies involving the differentiation or separation of the effects of cerebral iron and myelin content may benefit from a combination of R2* mapping and QSM (Deistung et al., 2013; Wisnieff et al., 2015) because iron content is paramagnetic and myelin is diamagnetic, while both can increase the R2* (Deistung et al., 2013; Langkammer et al., 2012a; Lee et al., 2012b). Using R2* mapping and QSM together, the investigation of the properties of tissue and the underlying pathological mechanisms becomes possible. The advantages of the joint use of R2* and QSM have been demonstrated in several recent studies focusing on MS lesions (Li et al., 2016; Zhang

et al., 2016; Harrison et al., 2016). However, care should be taken when interpreting the R2* and QSM results in the white matter, since both R2* and susceptibility may be dependent on fiber orientation (Li et al., 2012; Lee et al., 2011b; Rudko et al., 2014; Wharton and Bowtell, 2013; He and Yablonskiy, 2009).

Furthermore, as seen in Table 1, there is a clear and strong linear correlation between both QSM and R2* with direct measurements of iron concentration in the brain, validated by several in vivo and in vitro studies over the past decade (Liu et al., 2016a; Barbosa et al., 2015; Schweser et al., 2011; Shmueli et al., 2009; Langkammer et al., 2010, 2012a, 2012b; Zheng et al., 2013; Xia et al., 2015; He et al., 2015; Yao et al., 2009; Ning et al., 2014; Uddin et al., 2016; Martin et al., 2008; Peran et al., 2009; Yan et al., 2012; Sedlacik et al., 2014; Bilgic et al., 2012; Persson et al., 2015; Lim et al., 2013; Chai et al., 2015; Wharton and Bowtell, 2010). This implies that with R2* (being careful to use the conversion factor at a given field strength) and susceptibility mapping techniques abnormal iron levels in the brain structures of neurodegenerative diseases such as MS and PD can be converted to elevated levels of actual iron concentration in different regions of a diseased brain.

For the quantification of iron outside the brain, such as liver and heart, R2* mapping is still the most popular method. This popularity can be attributed to the validation of R2* mapping via biopsy, the sensitivity of R2* to changes in iron content, and the dynamic range of R2* mapping, especially at 1.5 T.

With the advent of higher field strengths, better coils, and stronger gradients, the ability to visualize tissue types clearly with high resolution and high SNR has dramatically improved. These technical advances, along with the appropriate imaging techniques and reconstruction algorithms such as source imaging using QSM, have made it possible to quantify many tissue characteristics including iron content using MRI.

References

Aboody, K.S., Bush, R.A., Garcia, E., et al., 2006. Development of a tumor-selective approach to treat metastatic cancer. PLoS One 1, e23.

Aboody, K.S., Najbauer, J., Schmidt, N.O., et al., 2006. Targeting of melanoma brain metastases using engineered neural stem/progenitor cells. Neuro-oncology 8 (2), 119–126.

Acosta-Cabronero, J., Cardenas-Blanco, A., Betts, M.J., et al., 2017. The whole-brain pattern of magnetic susceptibility perturbations in Parkinson's disease. Brain 140 (Pt 1), 118–131.

Aisen, P., Enns, C., Wessling-Resnick, M., 2001. Chemistry and biology of eukaryotic iron metabolism. Int. J. Biochem. Cell. Biol. 33 (10), 940–959.

Anderson, L.J., 2011. Assessment of iron overload with T2* magnetic resonance imaging. Prog. Cardiovasc. Dis. 54 (3), 287–294.

Anderson, L.J., Holden, S., Davis, B., et al., 2001. Cardiovascular T2-star (T2*) magnetic resonance for the early diagnosis of myocardial iron overload. Eur. Heart J. 22 (23), 2171–2179.

Arbab, A.S., Wilson, L.B., Ashari, P., Jordan, E.K., Lewis, B.K., Frank, J.A., 2005. A model of lysosomal metabolism of dextran coated superparamagnetic iron oxide (SPIO) nanoparticles: implications for cellular magnetic resonance imaging. NMR Biomed. 18 (6), 383–389.

Arosio, P., Levi, S., 2002. Ferritin, iron homeostasis, and oxidative damage. Free Radic. Biol. Med. 33 (4), 457–463.

Ayton, S., Lei, P., 2014. Nigral iron elevation is an invariable feature of Parkinson's disease and is a sufficient cause of neurodegeneration. Biomed. Res. Int. 2014, 581256.

Azuma, M., Hirai, T., Yamada, K., et al., 2016. Lateral asymmetry and spatial difference of iron deposition in the substantia nigra of patients with Parkinson disease measured with quantitative susceptibility mapping. AJNR Am. J. Neuroradiol. 37 (5), 782–788.

Bao, L., Li, X., Cai, C., Chen, Z., van Zijl, P.C., 2016. Quantitative susceptibility mapping using structural feature based collaborative reconstruction (SFCR) in the human brain. IEEE Trans. Med. Imag. 35 (9), 2040–2050.

Barbosa, J.H., Santos, A.C., Tumas, V., et al., 2015. Quantifying brain iron deposition in patients with Parkinson's disease using quantitative susceptibility mapping, R2 and R2. Magn. Reson. Imag. 33 (5), 559–565.

Bartzokis, G., Aravagiri, M., Oldendorf, W.H., Mintz, J., Marder, S.R., 1993. Field dependent transverse relaxation rate increase may be a specific measure of tissue iron stores. Magn. Reson. Med. Off. J. Soc. Magn. Reson. Med./Soc. Magn. Reson. Med. 29 (4), 459–464.

Bian, W., Harter, K., Hammond-Rosenbluth, K.E., et al., 2013. A serial in vivo 7T magnetic resonance phase imaging study of white matter lesions in multiple sclerosis. Mult. Scler. 19 (1), 69–75.

Bilgic, B., Pfefferbaum, A., Rohlfing, T., Sullivan, E.V., Adalsteinsson, E., 2012. MRI estimates of brain iron concentration in normal aging using quantitative susceptibility mapping. NeuroImage 59 (3), 2625–2635.

Bowen, C.V., Zhang, X., Saab, G., Gareau, P.J., Rutt, B.K., 2002. Application of the static dephasing regime theory to superparamagnetic iron-oxide loaded cells. Magn. Reson. Med. Off. J. Soc. Magn. Reson. Med./Soc. Magn. Reson. Med. 48 (1), 52–61.

Brown, R.W., Cheng, Y.-C.N., Haacke, E.M., Thompson, M.R., Venkatesan, R., 2014. Magnetic Resonance Imaging : Physical Principles and Sequence Design, second ed. John Wiley & Sons, Inc., Hoboken, New Jersey.

Bull, E., Madani, S.Y., Sheth, R., Seifalian, A., Green, M., Seifalian, A.M., 2014. Stem cell tracking using iron oxide nanoparticles. Int. J. Nanomed. 9, 1641–1653.

Campan, M., Lionetti, V., Aquaro, G.D., et al., 2011. Ferritin as a reporter gene for in vivo tracking of stem cells by 1.5-T cardiac MRI in a rat model of myocardial infarction. Am. J. Physiol. Heart Circ. Physiol. 300 (6), H2238–H2250.

Carpenter, J.P., He, T., Kirk, P., et al., 2011. On T2* magnetic resonance and cardiac iron. Circulation 123 (14), 1519–1528.

Chai, C., Yan, S., Chu, Z., et al., 2015. Quantitative measurement of brain iron deposition in patients with haemodialysis using susceptibility mapping. Metab. Brain Dis. 30 (2), 563–571.

Chawla, S., Kister, I., Wuerfel, J., et al., 2016. Iron and non-iron-related characteristics of multiple sclerosis and neuromyelitis optica lesions at 7T MRI. AJNR Am. J. Neuroradiol. 37 (7), 1223–1230.

Chen, W., Gauthier, S.A., Gupta, A., et al., 2014. Quantitative susceptibility mapping of multiple sclerosis lesions at various ages. Radiology 271 (1), 183–192.

Chen, Y., Liu, S., Wang, Y., Kang, Y., Haacke, E.M., 2018. STrategically Acquired Gradient Echo (STAGE) imaging, part I: creating enhanced T1 contrast and standardized susceptibility weighted imaging and quantitative susceptibility mapping. Magn. Reson. Imag. 46, 130–139.

Cheng, Y.C., Neelavalli, J., Haacke, E.M., 2009. Limitations of calculating field distributions and magnetic susceptibilities in MRI using a Fourier based method. Phys. Med. Biol. 54 (5), 1169–1189.

Cheung, J.S., Chow, A.M., Hui, E.S., Yang, J., Tse, H.F., Wu, E.X., 2006. Cell number quantification of USPIO-labeled stem cells by MRI: an in vitro study. In: Conference Proceedings : Annual International Conference of the IEEE Engineering in Medicine and Biology Society IEEE Engineering in Medicine and Biology Society Annual Conference, vol. 1, pp. 476–479.

Chu, Z., Cohen, A.R., Muthupillai, R., Chung, T., Wang, Z.J., 2004. MRI measurement of hepatic magnetic susceptibility-phantom validation and normal subject studies. Magn. Reson. Med. Off. J. Soc. Magn. Reson. Med./Soc. Magn. Reson. Med. 52 (6), 1318–1327.

Cohen, B., Dafni, H., Meir, G., Harmelin, A., Neeman, M., 2005. Ferritin as an endogenous MRI reporter for noninvasive imaging of gene expression in C6 glioma tumors. Neoplasia 7 (2), 109–117.

Cohen, B., Ziv, K., Plaks, V., et al., 2007. MRI detection of transcriptional regulation of gene expression in transgenic mice. Nat. Med. 13 (4), 498–503.

Cronin, M.J., Wharton, S., Al-Radaideh, A., et al., 2016. A comparison of phase imaging and quantitative susceptibility mapping in the imaging of multiple sclerosis lesions at ultrahigh field. Magma 29 (3), 543–557.

Danks, M.K., Yoon, K.J., Bush, R.A., et al., 2007. Tumor-targeted enzyme/prodrug therapy mediates long-term disease-free survival of mice bearing disseminated neuroblastoma. Canc. Res. 67 (1), 22–25.

Dashtipour, K., Liu, M., Kani, C., et al., 2015. Iron accumulation is not homogenous among patients with Parkinson's disease. Park. Dis. 2015, 324843.

Deans, A.E., Wadghiri, Y.Z., Bernas, L.M., Yu, X., Rutt, B.K., Turnbull, D.H., 2006. Cellular MRI contrast via coexpression of transferrin receptor and ferritin. Magn. Reson. Med. 56 (1), 51–59.

Deborah Chirnomas, S., Geukes-Foppen, M., Barry, K., et al., 2008. Practical implications of liver and heart iron load assessment by T2*-MRI in children and adults with transfusion-dependent anemias. Am. J. Hematol. 83 (10), 781–783.

Deistung, A., Schafer, A., Schweser, F., Biedermann, U., Turner, R., Reichenbach, J.R., 2013. Toward in vivo histology: a comparison of quantitative susceptibility mapping (QSM) with magnitude-, phase-, and R2*-imaging at ultra-high magnetic field strength. NeuroImage 65, 299–314.

Deistung, A., Schweser, F., Reichenbach, J.R., 2017. Overview of quantitative susceptibility mapping. NMR Biomed. 30 (4).

Du, G., Lewis, M.M., Styner, M., et al., 2011. Combined R2* and diffusion tensor imaging changes in the substantia nigra in Parkinson's disease. Mov. Disord. 26 (9), 1627–1632.

Du, G., Liu, T., Lewis, M.M., et al., 2016. Quantitative susceptibility mapping of the midbrain in Parkinson's disease. Mov. Disord. 31 (3), 317–324.

Economopoulos, V., Chen, Y., McFadden, C., Foster, P.J., 2013. MRI detection of nonproliferative tumor cells in lymph node metastases using iron oxide particles in a mouse model of breast cancer. Transl. Oncol. 6 (3), 347–354.

Eskreis-Winkler, S., Deh, K., Gupta, A., et al., 2015. Multiple sclerosis lesion geometry in quantitative susceptibility mapping (QSM) and phase imaging. J. Magn. Reson. Imag. JMRI 42 (1), 224–229.

Esterhammer, R., Seppi, K., Reiter, E., et al., 2015. Potential of diffusion tensor imaging and relaxometry for the detection of specific pathological alterations in Parkinson's disease (PD). PLoS One 10 (12), e0145493.

FDA Drug Safety Communication, 2015. FDA strengthens warnings and changes prescribing instructions to decrease the risk of serious allergic reactions with anemia drug Feraheme (ferumoxytol). https://www.fda.gov/Drugs/DrugSafety/ucm440138.htm.

Feng, Y., Liu, Q., Zhu, J., Xie, F., Li, L., 2012. Efficiency of ferritin as an MRI reporter gene in NPC cells is enhanced by iron supplementation. J. Biomed. Biotechnol. 2012, 434878.

Feng, W., Xuan, Y., Haacke, E., 2013. Expansion of the GESFIDE sequence for simultaneous SWI, T1W imaging and MR Angiography. In: Paper Presented at: Proc. Intl. Soc. Mag. Reson. Med.

Feng, Y., He, T., Carpenter, J.P., et al., 2013. In vivo comparison of myocardial T1 with T2 and T2* in thalassaemia major. J. Magn. Reson. Imag. JMRI 38 (3), 588–593.
Finn, J.P., Nguyen, K.L., Hu, P., 2017. Ferumoxytol vs. Gadolinium agents for contrast-enhanced MRI: thoughts on evolving indications, risks, and benefits. J. Magn. Reson. Imag. JMRI 46 (3), 919–923.
Fragasso, A., Ciancio, A., Mannarella, C., et al., 2011. Myocardial iron overload assessed by magnetic resonance imaging (MRI)T2* in multi-transfused patients with thalassemia and acquired anemias. Eur. J. Intern. Med. 22 (1), 62–65.
Friedman, A., Arosio, P., Finazzi, D., Koziorowski, D., Galazka-Friedman, J., 2011. Ferritin as an important player in neurodegeneration. Park. Relat. D. 17 (6), 423–430.
Gambarota, G., van Laarhoven, H.W., Philippens, M., et al., 2006. Assessment of absolute blood volume in carcinoma by USPIO contrast-enhanced MRI. Magn. Reson. Imag. 24 (3), 279–286.
Gaudet, J.M., Hamilton, A.M., Chen, Y., Fox, M.S., Foster, P.J., 2016. Application of dual 19 F and iron cellular MRI agents to track the infiltration of immune cells to the site of a rejected stem cell transplant. Magn. Reson. Med. 78 (2), 713–720.
Ge, Y., Jensen, J.H., Lu, H., et al., 2007. Quantitative assessment of iron accumulation in the deep gray matter of multiple sclerosis by magnetic field correlation imaging. AJNR Am. J. Neuroradiol. 28 (9), 1639–1644.
Gharagouzloo, C.A., McMahon, P.N., Sridhar, S., 2015. Quantitative contrast-enhanced MRI with superparamagnetic nanoparticles using ultrashort time-to-echo pulse sequences. Magn. Reson. Med. Off. J. Soc. Magn. Reson. Med./Soc. Magn. Reson. Med. 74 (2), 431–441.
Ghugre, N.R., Enriquez, C.M., Gonzalez, I., Nelson Jr., M.D., Coates, T.D., Wood, J.C., 2006. MRI detects myocardial iron in the human heart. Magn. Reson. Med. Off. J. Soc. Magn. Reson. Med./Soc. Magn. Reson. Med. 56 (3), 681–686.
Girard, O.M., Ramirez, R., McCarty, S., Mattrey, R.F., 2012. Toward absolute quantification of iron oxide nanoparticles as well as cell internalized fraction using multiparametric MRI. Contrast Media Mol. Imag. 7 (4), 411–417.
Gorell, J.M., Ordidge, R.J., Brown, G.G., Deniau, J.C., Buderer, N.M., Helpern, J.A., 1995. Increased iron-related MRI contrast in the substantia nigra in Parkinson's disease. Neurology 45 (6), 1138–1143.
Granot, D., Nkansah, M.K., Bennewitz, M.F., Tang, K.S., Markakis, E.A., Shapiro, E.M., 2013. Clinically viable magnetic poly(lactide-co-glycolide) particles for MRI-based cell tracking. Magn. Reson. Med.
Guan, X., Xuan, M., Gu, Q., et al., 2017. Regionally progressive accumulation of iron in Parkinson's disease as measured by quantitative susceptibility mapping. NMR Biomed. 30 (4).
Guan, X., Xuan, M., Gu, Q., et al., 2017. Influence of regional iron on the motor impairments of Parkinson's disease: a quantitative susceptibility mapping study. J. Magn. Reson. Imag. JMRI 45 (5), 1335–1342.
Guo, J.H., Juan, S.H., Aust, S.D., 1998. Suppression of cell growth by heavy chain ferritin. Biochem. Biophys. Res. Commun. 242 (1), 39–45.
Gutova, M., Frank, J.A., D'Apuzzo, M., et al., 2013. Magnetic resonance imaging tracking of ferumoxytol-labeled human neural stem cells: studies leading to clinical use. Stem Cells Transl. Med. 2 (10), 766–775.
Haacke, E.M., 1999. Magnetic Resonance Imaging : Physical Principles and Sequence Design. Wiley, New York.
Haacke, E.M., Xu, Y., Cheng, Y.C., Reichenbach, J.R., 2004. Susceptibility weighted imaging (SWI). Magn. Reson. Med. Off. J. Soc. Magn. Reson. Med./Soc. Magn. Reson. Med. 52 (3), 612–618.
Haacke, E.M., Cheng, N.Y., House, M.J., et al., 2005. Imaging iron stores in the brain using magnetic resonance imaging. Magn. Reson. Imag. 23 (1), 1–25.
Haacke, E.M., Ayaz, M., Khan, A., et al., 2007. Establishing a baseline phase behavior in magnetic resonance imaging to determine normal vs. abnormal iron content in the brain. J. Magn. Reson. Imag. JMRI 26 (2), 256–264.
Haacke, E.M., Makki, M., Ge, Y., et al., 2009. Characterizing iron deposition in multiple sclerosis lesions using susceptibility weighted imaging. J. Magn. Reson. Imag. JMRI 29 (3), 537–544.
Haacke, E.M., Miao, Y., Liu, M., et al., 2010. Correlation of putative iron content as represented by changes in R2* and phase with age in deep gray matter of healthy adults. J. Magn. Reson. Imag. JMRI 32 (3), 561–576.
Haacke, E.M., Tang, J., Neelavalli, J., Cheng, Y.C., 2010. Susceptibility mapping as a means to visualize veins and quantify oxygen saturation. J. Magn. Reson. Imag. JMRI 32 (3), 663–676.
Haacke, E.M., Liu, S., Buch, S., Zheng, W., Wu, D., Ye, Y., 2015. Quantitative susceptibility mapping: current status and future directions. Magn. Reson. Imag. 33 (1), 1–25.
Habib, C.A., Zheng, W., Haacke, E.M., Webb, S., Nichol, H., 2010. Visualizing iron deposition in multiple sclerosis cadaver brains. In: 6th International Conference on Medical Applications of Synchrotron Radiation.
Habib, C.A., Liu, M., Bawany, N., et al., 2012. Assessing abnormal iron content in the deep gray matter of patients with multiple sclerosis versus healthy controls. AJNR Am. J. Neuroradiol. 33 (2), 252–258.
Hagemeier, J., Heininen-Brown, M., Poloni, G.U., et al., 2012. Iron deposition in multiple sclerosis lesions measured by susceptibility-weighted imaging filtered phase: a case control study. J. Magn. Reson. Imag. JMRI 36 (1), 73–83.
Hallgren, B., Sourander, P., 1958. The effect of age on the non-haemin iron in the human brain. J. Neurochem. 3 (1), 41–51.
Hamilton, J.I., Jiang, Y., Chen, Y., et al., 2017. MR fingerprinting for rapid quantification of myocardial T1, T2, and proton spin density. Magn. Reson. Med. Off. J. Soc. Magn. Reson. Med./Soc. Magn. Reson. Med. 77 (4), 1446–1458.
Hammond, K.E., Metcalf, M., Carvajal, L., et al., 2008. Quantitative in vivo magnetic resonance imaging of multiple sclerosis at 7 Tesla with sensitivity to iron. Ann. Neurol. 64 (6), 707–713.
Han, S.H., Cho, J.H., Jung, H.S., et al., 2015. Robust MR assessment of cerebral blood volume and mean vessel size using SPION-enhanced ultrashort echo acquisition. NeuroImage 112, 382–389.
Harrison, D.M., Li, X., Liu, H., et al., 2016. Lesion heterogeneity on high-field susceptibility MRI is associated with multiple sclerosis severity. AJNR Am. J. Neuroradiol. 37 (8), 1447–1453.
Hasegawa, S., Morokoshi, Y., Kanda, H., et al., 2012. H-ferritin overexpression promotes radiation-induced leukemia/lymphoma in mice. Carcinogenesis 33 (11), 2269–2275.
He, X., Yablonskiy, D.A., 2009. Biophysical mechanisms of phase contrast in gradient echo MRI. Proc. Natl. Acad. Sci. U. S. A. 106 (32), 13558–13563.
He, N., Ling, H., Ding, B., et al., 2015. Region-specific disturbed iron distribution in early idiopathic Parkinson's disease measured by quantitative susceptibility mapping. Hum. Brain Mapp. 36 (11), 4407–4420.
He, N., Huang, P., Ling, H., et al., 2017. Dentate nucleus iron deposition is a potential biomarker for tremor-dominant Parkinson's disease. NMR Biomed. 30 (4).
Hernando, D., Kuhn, J.P., Mensel, B., et al., 2013. R2* estimation using "in-phase" echoes in the presence of fat: the effects of complex spectrum of fat. J. Magn. Reson. Imag. JMRI 37 (3), 717–726.
Hernando, D., Kramer, J.H., Reeder, S.B., 2013. Multipeak fat-corrected complex R2* relaxometry: theory, optimization, and clinical validation. Magn. Reson. Med. Off. J. Soc. Magn. Reson. Med./Soc. Magn. Reson. Med. 70 (5), 1319–1331.
Hernando, D., Cook, R.J., Diamond, C., Reeder, S.B., Hernando, D., Cook, R.J., Diamond, C., Reeder, S.B., 2013. Magnetic susceptibility as a B0 field strength independent MRI biomarker of liver iron overload. Magn. Reson. Med. 70, 648–656.
Hernando, D., Levin, Y.S., Sirlin, C.B., Reeder, S.B., 2014. Quantification of liver iron with MRI: state of the art and remaining challenges. J. Magn. Reson. Imag. JMRI 40 (5), 1003–1021.
Higuchi, T., Anton, M., Dumler, K., et al., 2009. Combined reporter gene PET and iron oxide MRI for monitoring survival and localization of transplanted cells in the rat heart. J. Nucl. Med. 50 (7), 1088–1094.
Hong, W., He, Q., Fan, S., et al., 2017. Imaging and quantification of iron-oxide nanoparticles (IONP) using MP-RAGE and UTE based sequences. Magn. Reson. Med. Off. J. Soc. Magn. Reson. Med./Soc. Magn. Reson. Med. 78 (1), 226–232.
Hopes, L., Grolez, G., Moreau, C., et al., 2016. Magnetic resonance imaging features of the nigrostriatal system: biomarkers of Parkinson's disease stages? PLoS One 11 (4), e0147947.
Hopp, K., Popescu, B.F., McCrea, R.P., et al., 2010. Brain iron detected by SWI high pass filtered phase calibrated with synchrotron X-ray fluorescence. J. Magn. Reson. Imag. JMRI 31 (6), 1346–1354.
Jensen, J.H., Szulc, K., Hu, C., et al., 2009. Magnetic field correlation as a measure of iron-generated magnetic field inhomogeneities in the brain. Magn. Reson. Med. Sci. 61 (2), 481–485.
Ji, S., Zhang, S., Mao, Z., et al., 2016. Quantitative assessment of iron deposition in Parkinson's disease using enhanced T2 star-weighted angiography. Neurol. India 64 (3), 428–435.
Jiang, C., Wu, D., Haacke, E.M., 2017. Ferritin-EGFP chimera as an endogenous dual-reporter for both fluorescent and magnetic resonance imaging in human glioma U251 cells. Tomography 3 (1), 8.
Kanda, T., Ishii, K., Kawaguchi, H., Kitajima, K., Takenaka, D., 2014. High signal intensity in the dentate nucleus and globus pallidus on unenhanced T1-weighted MR images: relationship with increasing cumulative dose of a gadolinium-based contrast material. Radiology 270 (3), 834–841.
Kanda, T., Oba, H., Toyoda, K., Kitajima, K., Furui, S., 2016. Brain gadolinium deposition after administration of gadolinium-based contrast agents. Jpn. J. Radiol. 34 (1), 3–9.
Kasten, A., Gruttner, C., Kuhn, J.P., Bader, R., Pasold, J., Frerich, B., 2014. Comparative in vitro study on magnetic iron oxide nanoparticles for MRI tracking of adipose tissue-derived progenitor cells. PLoS One 9 (9), e108055.
Kedziorek, D.A., Kraitchman, D.L., 2010. Superparamagnetic iron oxide labeling of stem cells for MRI tracking and delivery in cardiovascular disease. Meth. Mol. Biol. 660, 171–183.
Kim, H.S., Cho, H.R., Choi, S.H., Woo, J.S., Moon, W.K., 2010. In vivo imaging of tumor transduced with bimodal lentiviral vector encoding human ferritin and green fluorescent protein on a 1.5T clinical magnetic resonance scanner. Canc. Res. 70 (18), 7315–7324.
Kim, S.G., Harel, N., Jin, T., Kim, T., Lee, P., Zhao, F., 2013. Cerebral blood volume MRI with intravascular superparamagnetic iron oxide nanoparticles. NMR Biomed. 26 (8), 949–962.
Kim, S.J., Lewis, B., Steiner, M.S., Bissa, U.V., Dose, C., Frank, J.A., 2016. Superparamagnetic iron oxide nanoparticles for direct labeling of stem cells and in vivo MRI tracking. Contrast Media Mol. Imag. 11 (1), 55–64.
Kokeny, P., Cheng, Y.N., Liu, S., Xie, H., Jiang, Q., 2017. Quantifications of in vivo labeled stem cells based on measurements of magnetic moments. Magn. Reson. Imag. 35, 141–147.
Krafft, A.J., Loeffler, R.B., Song, R., et al., 2016. Does fat suppression via chemically selective saturation affect R2*-MRI for transfusional iron overload assessment? A clinical evaluation at 1.5T and 3T. Magn. Reson. Med. Off. J. Soc. Magn. Reson. Med./Soc. Magn. Reson. Med. 76 (2), 591–601.
Kutzelnigg, A., Lassmann, H., 2014. Pathology of multiple sclerosis and related inflammatory demyelinating diseases. Handb. Clin. Neurol. 122, 15–58.
Langkammer, C., Krebs, N., Goessler, W., et al., 2010. Quantitative MR imaging of brain iron: a postmortem validation study. Radiology 257 (2), 455–462.
Langkammer, C., Krebs, N., Goessler, W., et al., 2012. Susceptibility induced gray-white matter MRI contrast in the human brain. NeuroImage 59 (2), 1413–1419.
Langkammer, C., Schweser, F., Krebs, N., et al., 2012. Quantitative susceptibility mapping (QSM) as a means to measure brain iron? A post mortem validation study. NeuroImage 62 (3), 1593–1599.

Langkammer, C., Liu, T., Khalil, M., et al., 2013. Quantitative susceptibility mapping in multiple sclerosis. Radiology 267 (2), 551–559.
Langkammer, C., Pirpamer, L., Seiler, S., et al., 2016. Quantitative susceptibility mapping in Parkinson's disease. PLoS One 11 (9), e0162460.
Langkammer, C., Schweser, F., Shmueli, K., et al., 2017. Quantitative susceptibility mapping: report from the 2016 reconstruction challenge. Magn. Reson. Med. Off. J. Soc. Magn. Reson. Med./Soc. Magn. Reson. Med.
Leder, A., Raschzok, N., Schmidt, C., et al., 2015. Micron-sized iron oxide-containing particles for microRNA-targeted manipulation and MRI-based tracking of transplanted cells. Biomaterials 51, 129–137.
Lee, N., Kim, H., Choi, S.H., et al., 2011. Magnetosome-like ferrimagnetic iron oxide nanocubes for highly sensitive MRI of single cells and transplanted pancreatic islets. Proc. Natl. Acad. Sci. U. S. A. 108 (7), 2662–2667.
Lee, J., van Gelderen, P., Kuo, L.W., Merkle, H., Silva, A.C., Duyn, J.H., 2011. T2*-based fiber orientation mapping. NeuroImage 57 (1), 225–234.
Lee, H.J., Won, J.H., Doo, S.H., et al., 2012. Inhibition of collagen deposit in obstructed rat bladder outlet by transplantation of superparamagnetic iron oxide-labeled human mesenchymal stem cells as monitored by molecular magnetic resonance imaging (MRI). Cell. Transplant. 21 (5), 959–970.
Lee, J., Shmueli, K., Kang, B.T., et al., 2012. The contribution of myelin to magnetic susceptibility-weighted contrasts in high-field MRI of the brain. NeuroImage 59 (4), 3967–3975.
Li, W., Wu, B., Liu, C., 2011. Quantitative susceptibility mapping of human brain reflects spatial variation in tissue composition. NeuroImage 55 (4), 1645–1656.
Li, W., Wu, B., Avram, A.V., Liu, C., 2012. Magnetic susceptibility anisotropy of human brain in vivo and its molecular underpinnings. NeuroImage 59 (3), 2088–2097.
Li, X.X., Li, K.A., Qin, J.B., et al., 2013. In vivo MRI tracking of iron oxide nanoparticle-labeled human mesenchymal stem cells in limb ischemia. Int. J. Nanomed. 8, 1063–1073.
Li, W., Wu, B., Batrachenko, A., et al., 2014. Differential developmental trajectories of magnetic susceptibility in human brain gray and white matter over the lifespan. Hum. Brain Mapp. 35 (6), 2698–2713.
Li, W., Avram, A.V., Wu, B., Xiao, X., Liu, C., 2014. Integrated Laplacian-based phase unwrapping and background phase removal for quantitative susceptibility mapping. NMR Biomed. 27 (2), 219–227.
Li, X., Harrison, D.M., Liu, H., et al., 2016. Magnetic susceptibility contrast variations in multiple sclerosis lesions. J. Magn. Reson. Imag. JMRI 43 (2), 463–473.
Lim, I.A., Faria, A.V., Li, X., et al., 2013. Human brain atlas for automated region of interest selection in quantitative susceptibility mapping: application to determine iron content in deep gray matter structures. NeuroImage 82, 449–469.
Liu, T., Khalidov, I., de Rochefort, L., et al., 2011. A novel background field removal method for MRI using projection onto dipole fields (PDF). NMR Biomed. 24 (9), 1129–1136.
Liu, J., Liu, T., de Rochefort, L., et al., 2012. Morphology enabled dipole inversion for quantitative susceptibility mapping using structural consistency between the magnitude image and the susceptibility map. NeuroImage 59 (3), 2560–2568.
Liu, S., Mok, K., Neelavalli, J., et al., 2014. Improved MR venography using quantitative susceptibility-weighted imaging. J. Magn. Reson. Imag. JMRI 40 (3), 698–708.
Liu, C., Li, W., Tong, K.A., Yeom, K.W., Kuzminski, S., 2015. Susceptibility-weighted imaging and quantitative susceptibility mapping in the brain. J. Magn. Reson. Imag. JMRI 42 (1), 23–41.
Liu, M., Liu, S., Ghassaban, K., et al., 2016. Assessing global and regional iron content in deep gray matter as a function of age using susceptibility mapping. J. Magn. Reson. Imag. JMRI 44 (1), 59–71.
Liu, S., Wang, C., Zhang, X., et al., 2016. Quantification of liver iron concentration using the apparent susceptibility of vessels. In: Paper Presented at: Proc. 24th Annu. Meet. ISMRM Singap.
Liu, S., Buch, S., Chen, Y., et al., 2017. Susceptibility-weighted imaging: current status and future directions. NMR Biomed. 30 (4).
Liu, S., Brisset, J.C., Hu, J., Haacke, E.M., Ge, Y., 2017. Susceptibility weighted imaging and quantitative susceptibility mapping of the cerebral vasculature using ferumoxytol. J. Magn. Reson. Imag. JMRI.
Long, Q., Li, J., Luo, Q., et al., 2015. MRI tracking of bone marrow mesenchymal stem cells labeled with ultra-small superparamagnetic iron oxide nanoparticles in a rat model of temporal lobe epilepsy. Neurosci. Lett. 606, 30–35.
Lotfipour, A.K., Wharton, S., Schwarz, S.T., et al., 2012. High resolution magnetic susceptibility mapping of the substantia nigra in Parkinson's disease. J. Magn. Reson. Imag. JMRI 35 (1), 48–55.
Luo, J., He, X., Yablonskiy, D.A., 2014. Magnetic susceptibility induced white matter MR signal frequency shifts–experimental comparison between Lorentzian sphere and generalized Lorentzian approaches. Magn. Reson. Med. Off. J. Soc. Magn. Reson. Med./Soc. Magn. Reson. Med. 71 (3), 1251–1263.
Ma, J., Wehrli, F.W., 1996. Method for image-based measurement of the reversible and irreversible contribution to the transverse-relaxation rate. J. Magn. Reson. B 111 (1), 61–69.
Mani, V., Adler, E., Briley-Saebo, K.C., et al., 2008. Serial in vivo positive contrast MRI of iron oxide-labeled embryonic stem cell-derived cardiac precursor cells in a mouse model of myocardial infarction. Magn. Reson. Med. 60 (1), 73–81.
Martin, W.R., Wieler, M., Gee, M., 2008. Midbrain iron content in early Parkinson disease: a potential biomarker of disease status. Neurology 70 (16 Pt 2), 1411–1417.
Martin-Bastida, A., Lao-Kaim, N.P., Loane, C., et al., 2017. Motor associations of iron accumulation in deep grey matter nuclei in Parkinson's disease: a cross-sectional study of iron-related magnetic resonance imaging susceptibility. Eur. J. Neurol. 24 (2), 357–365.
Mavrogeni, S.I., Markussis, V., Kaklamanis, L., et al., 2005. A comparison of magnetic resonance imaging and cardiac biopsy in the evaluation of heart iron overload in patients with beta-thalassemia major. Eur. J. Haematol. 75 (3), 241–247.
Mehta, V., Pei, W., Yang, G., et al., 2013. Iron is a sensitive biomarker for inflammation in multiple sclerosis lesions. PLoS One 8 (3), e57573.
Mishra, S.K., Khushu, S., Gangenahalli, G., 2017. Biological effects of iron oxide-protamine sulfate complex on mesenchymal stem cells and its relaxometry based labeling optimization for cellular MRI. Exp. Cell. Res. 351 (1), 59–67.
Murakami, Y., Kakeda, S., Watanabe, K., et al., 2015. Usefulness of quantitative susceptibility mapping for the diagnosis of Parkinson disease. AJNR Am. J. Neuroradiol. 36 (6), 1102–1108.
Ning, N., Zhang, L., Gao, J., et al., 2014. Assessment of iron deposition and white matter maturation in infant brains by using enhanced T2 star weighted angiography (ESWAN): R2* versus phase values. PLoS One 9 (2), e89888.
Noad, J., Gonzalez-Lara, L.E., Broughton, H.C., et al., 2013. MRI tracking of transplanted iron-labeled mesenchymal stromal cells in an immune-compromised mouse model of critical limb ischemia. NMR Biomed. 26 (4), 458–467.
Ono, K., Fuma, K., Tabata, K., Sawada, M., 2009. Ferritin reporter used for gene expression imaging by magnetic resonance. Biochem. Biophys. Res. Commun. 388 (3), 589–594.
Pawelczyk, E., Arbab, A.S., Pandit, S., Hu, E., Frank, J.A., 2006. Expression of transferrin receptor and ferritin following ferumoxides-protamine sulfate labeling of cells: implications for cellular magnetic resonance imaging. NMR Biomed. 19 (5), 581–592.
Peran, P., Cherubini, A., Luccichenti, G., et al., 2009. Volume and iron content in basal ganglia and thalamus. Hum. Brain Mapp. 30 (8), 2667–2675.
Peran, P., Cherubini, A., Assogna, F., et al., 2010. Magnetic resonance imaging markers of Parkinson's disease nigrostriatal signature. Brain 133 (11), 3423–3433.
Pereira, S.M., Moss, D., Williams, S.R., Murray, P., Taylor, A., 2015. Overexpression of the MRI reporter genes ferritin and transferrin receptor affect iron homeostasis and produce limited contrast in mesenchymal stem cells. Int. J. Mol. Sci. 16 (7), 15481–15496.
Persson, N., Wu, J., Zhang, Q., et al., 2015. Age and sex related differences in subcortical brain iron concentrations among healthy adults. NeuroImage 122, 385–398.
Pfefferbaum, A., Adalsteinsson, E., Rohlfing, T., Sullivan, E.V., 2009. MRI estimates of brain iron concentration in normal aging: comparison of field-dependent (FDRI) and phase (SWI) methods. NeuroImage 47 (2), 493–500.
Pietracupa, S., Martin-Bastida, A., Piccini, P., 2017. Iron metabolism and its detection through MRI in parkinsonian disorders: a systematic review. Neurol. Sci.
Polman, C.H., Reingold, S.C., Banwell, B., et al., 2011. Diagnostic criteria for multiple sclerosis: 2010 revisions to the McDonald criteria. Ann. Neurol. 69 (2), 292–302.
Potchen, M.J., Kampondeni, S.D., Seydel, K.B., et al., 2018. 1.5 Tesla magnetic resonance imaging to investigate potential etiologies of brain swelling in pediatric cerebral malaria. Am. J. Trop. Med. Hyg. 98 (2), 497–504.
Reddy, A.M., Kwak, B.K., Shim, H.J., et al., 2010. In vivo tracking of mesenchymal stem cells labeled with a novel chitosan-coated superparamagnetic iron oxide nanoparticles using 3.0T MRI. J. Kor. Med. Sci. 25 (2), 211–219.
Reichenbach, J.R., Schweser, F., Serres, B., Deistung, A., 2015. Quantitative susceptibility mapping: concepts and applications. Clin. Neuroradiol. 25 (Suppl. 2), 225–230.
Ribot, E.J., Foster, P.J., 2012. In vivo MRI discrimination between live and lysed iron-labelled cells using balanced steady state free precession. Eur. Radiol. 22 (9), 2027–2034.
Rossi, M., Ruottinen, H., Soimakallio, S., Elovaara, I., Dastidar, P., 2013. Clinical MRI for iron detection in Parkinson's disease. Clin. Imag. 37 (4), 631–636.
Rudko, D.A., Klassen, L.M., de Chickera, S.N., Gati, J.S., Dekaban, G.A., Menon, R.S., 2014. Origins of R2* orientation dependence in gray and white matter. Proc. Natl. Acad. Sci. U. S. A. 111 (1), E159–E167.
Ruggiero, A., Guenoun, J., Smit, H., et al., 2013. In vivo MRI mapping of iron oxide-labeled stem cells transplanted in the heart. Contrast Media Mol. Imag. 8 (6), 487–494.
Runge, J.H., Akkerman, E.M., Troelstra, M.A., Nederveen, A.J., Beuers, U., Stoker, J., 2016. Comparison of clinical MRI liver iron content measurements using signal intensity ratios, R 2 and R 2. Abdom. Radiol. (NY). 41 (11), 2123–2131.
Sado, D.M., Maestrini, V., Piechnik, S.K., et al., 2015. Noncontrast myocardial T1 mapping using cardiovascular magnetic resonance for iron overload. J. Magn. Reson. Imag. JMRI 41 (6), 1505–1511.
Salomir, R., de Senneville, B.D., Moonen, C.T., 2003. A fast calculation method for magnetic field inhomogeneity due to an arbitrary distribution of bulk susceptibility. Concepts Magn. Reson. Part B Magn. Reson. Eng. 19B, 26–34.
Schweser, F., Deistung, A., Lehr, B.W., Reichenbach, J.R., 2011. Quantitative imaging of intrinsic magnetic tissue properties using MRI signal phase: an approach to in vivo brain iron metabolism? NeuroImage 54 (4), 2789–2807.
Schweser, F., Sommer, K., Deistung, A., Reichenbach, J.R., 2012. Quantitative susceptibility mapping for investigating subtle susceptibility variations in the human brain. NeuroImage 62 (3), 2083–2100.
Sedlacik, J., Boelmans, K., Lobel, U., Holst, B., Siemonsen, S., Fiehler, J., 2014. Reversible, irreversible and effective transverse relaxation rates in normal aging brain at 3T. NeuroImage 84, 1032–1041.
Shahnaz, G., Kremser, C., Reinisch, A., et al., 2013. Efficient MRI labeling of endothelial progenitor cells: design of thiolated surface stabilized superparamagnetic iron oxide nanoparticles. Eur. J. Pharm. Biopharm. 85 (3 Pt A), 346–355.
Sharma, S.D., Hernando, D., Horng, D.E., Reeder, S.B., 2015. Quantitative susceptibility mapping in the abdomen as an imaging biomarker of hepatic iron overload. Magn. Reson. Med. Off. J. Soc. Magn. Reson. Med./Soc. Magn. Reson. Med. 74 (3), 673–683.
Sharma, S.D., Fischer, R., Schoennagel, B.P., et al., 2017. MRI-based quantitative susceptibility mapping (QSM) and R2* mapping of liver iron overload: comparison

with SQUID-based biomagnetic liver susceptometry. Magn. Reson. Med. Off. J. Soc. Magn. Reson. Med./Soc. Magn. Reson. Med. 78 (1), 264–270.
Shen, W.B., Vaccaro, D.E., Fishman, P.S., Groman, E.V., Yarowsky, P.S.I.R.B., 2016. Sans iron oxide rhodamine B, a novel cross-linked dextran nanoparticle, labels human neuroprogenitor and SH-SY5Y neuroblastoma cells and serves as a USPIO cell labeling control. Contrast Media Mol. Imag. 11 (3), 222–228.
Shichinohe, H., Kuroda, S., Kudo, K., et al., 2012. Visualization of the superparamagnetic iron oxide (SPIO)-Labeled bone marrow stromal cells using a 3.0-t MRI-a pilot study for clinical testing of neurotransplantation. Transl. Stroke Res. 3 (1), 99–106.
Shmueli, K., de Zwart, J.A., van Gelderen, P., Li, T.Q., Dodd, S.J., Duyn, J.H., 2009. Magnetic susceptibility mapping of brain tissue in vivo using MRI phase data. Magn. Reson. Med. Off. J. Soc. Magn. Reson. Med./Soc. Magn. Reson. Med. 62 (6), 1510–1522.
Smith, S.A., Bulte, J.W., van Zijl, P.C., 2009. Direct saturation MRI: theory and application to imaging brain iron. Magn. Reson. Med. Off. J. Soc. Magn. Reson. Med./Soc. Magn. Reson. Med. 62 (2), 384–393.
St Pierre, T.G., Clark, P.R., Chua-anusorn, W., et al., 2005. Noninvasive measurement and imaging of liver iron concentrations using proton magnetic resonance. Blood 105 (2), 855–861.
Stephenson, E., Nathoo, N., Mahjoub, Y., Dunn, J.F., Yong, V.W., 2014. Iron in multiple sclerosis: roles in neurodegeneration and repair. Nat. Rev. Neurol. 10 (8), 459–468.
Stojanov, D., Aracki-Trenkic, A., Benedeto-Stojanov, D., 2016. Gadolinium deposition within the dentate nucleus and globus pallidus after repeated administrations of gadolinium-based contrast agents-current status. Neuroradiology 58 (5), 433–441.
Storey, P., Thompson, A.A., Carqueville, C.L., Wood, J.C., de Freitas, R.A., Rigsby, C.K., 2007. R2* imaging of transfusional iron burden at 3T and comparison with 1.5T. J. Magn. Reson. Imag. JMRI 25 (3), 540–547.
Stuber, C., Pitt, D., Wang, Y., 2016. Iron in multiple sclerosis and its noninvasive imaging with quantitative susceptibility mapping. Int. J. Mol. Sci. 17 (1).
Sukstanskii, A.L., Yablonskiy, D.A., 2014. On the role of neuronal magnetic susceptibility and structure symmetry on gradient echo MR signal formation. Magn. Reson. Med. Off. J. Soc. Magn. Reson. Med./Soc. Magn. Reson. Med. 71 (1), 345–353.
Sun, H., Wilman, A.H., 2014. Background field removal using spherical mean value filtering and Tikhonov regularization. Magn. Reson. Med. Off. J. Soc. Magn. Reson. Med./Soc. Magn. Reson. Med. 71 (3), 1151–1157.
Tang, K.X., Shen, Y.F., Yang, X.B., et al., 2011. A study of tracking the superparamagnetic iron oxide and enhanced green fluorescent protein labeled miniature porcine bone marrow stem cells by in vitro MRI. Zhonghua nei ke za Zhi 50 (4), 322–327.
Tang, J., Liu, S., Neelavalli, J., Cheng, Y.C., Buch, S., Haacke, E.M., 2013. Improving susceptibility mapping using a threshold-based K-space/image domain iterative reconstruction approach. Magn. Reson. Med. Off. J. Soc. Magn. Reson. Med./Soc. Magn. Reson. Med. 69 (5), 1396–1407.
Taylor, B.A., Loeffler, R.B., Song, R., McCarville, M.B., Hankins, J.S., Hillenbrand, C.M., 2012. Simultaneous field and R2 mapping to quantify liver iron content using autoregressive moving average modeling. J. Magn. Reson. Imag. JMRI 35 (5), 1125–1132.
Tedeschi, E., Palma, G., Canna, A., et al., 2016. In vivo dentate nucleus MRI relaxometry correlates with previous administration of Gadolinium-based contrast agents. Eur. Radiol. 26 (12), 4577–4584.
Thu, M.S., Najbauer, J., Kendall, S.E., et al., 2009. Iron labeling and pre-clinical MRI visualization of therapeutic human neural stem cells in a murine glioma model. PLoS One 4 (9), e7218.
Thu, M.S., Bryant, L.H., Coppola, T., et al., 2012. Self-assembling nanocomplexes by combining ferumoxytol, heparin and protamine for cell tracking by magnetic resonance imaging. Nat. Med. 18 (3), 463–U165.
Toso, C., Vallee, J.P., Morel, P., et al., 2008. Clinical magnetic resonance imaging of pancreatic islet grafts after iron nanoparticle labeling. Am. J. Transplant. Off. J. Am. Soc. Transplant. Am. Soc. Transpl. Surg. 8 (3), 701–706.
Uddin, M.N., Lebel, R.M., Wilman, A.H., 2016. Value of transverse relaxometry difference methods for iron in human brain. Magn. Reson. Imag. 34 (1), 51–59.
Ulla, M., Bonny, J.M., Ouchchane, L., Rieu, I., Claise, B., Durif, F., 2013. Is R2* a new MRI biomarker for the progression of Parkinson's disease? A longitudinal follow-up. PLoS One 8 (3), e57904.
Vande Velde, G., Himmelreich, U., Neeman, M., 2013. Reporter gene approaches for mapping cell fate decisions by MRI: promises and pitfalls. Contrast Media Mol. Imag. 8 (6), 424–431.
Vandsburger, M.H., Radoul, M., Cohen, B., Neeman, M., 2013. MRI reporter genes: applications for imaging of cell survival, proliferation, migration and differentiation. NMR Biomed. 26 (7), 872–884.
Vasanawala, S.S., Nguyen, K.L., Hope, M.D., et al., 2016. Safety and technique of ferumoxytol administration for MRI. Magn. Reson. Med. Off. J. Soc. Magn. Reson. Med./Soc. Magn. Reson. Med. 75 (5), 2107–2111.
Vernikouskaya, I., Fekete, N., Bannwarth, M., et al., 2014. Iron-loaded PLLA nanoparticles as highly efficient intracellular markers for visualization of mesenchymal stromal cells by MRI. Contrast Media Mol. Imag. 9 (2), 109–121.
Vetter, A., Reinisch, A., Strunk, D., et al., 2011. Thiolated polyacrylic acid-modified iron oxide nanoparticles for in vitro labeling and MRI of stem cells. J. Drug Target. 19 (7), 562–572.
Vreys, R., Soenen, S.J., De Cuyper, M., Van der Linden, A., 2011. Background migration of USPIO/MLs is a major drawback for in situ labeling of endogenous neural progenitor cells. Contrast Media Mol. Imag. 6 (1), 1–6.
Walsh, A.J., Lebel, R.M., Eissa, A., et al., 2013. Multiple sclerosis: validation of MR imaging for quantification and detection of iron. Radiology 267 (2), 531–542.
Wang, Y., Liu, T., 2015. Quantitative susceptibility mapping (QSM): decoding MRI data for a tissue magnetic biomarker. Magn. Reson. Med. Off. J. Soc. Magn. Reson. Med./Soc. Magn. Reson. Med. 73 (1), 82–101.
Wang, Y., Butros, S.R., Shuai, X., et al., 2012. Different iron-deposition patterns of multiple system atrophy with predominant parkinsonism and idiopathetic Parkinson diseases demonstrated by phase-corrected susceptibility-weighted imaging. AJNR Am. J. Neuroradiol. 33 (2), 266–273.
Wang, Q., Li, K., Quan, Q., Zhang, G., 2014. R2* and R2 mapping for quantifying recruitment of superparamagnetic iron oxide-tagged endothelial progenitor cells to injured liver: tracking in vitro and in vivo. Int. J. Nanomed. 9, 1815–1822.
Wang, J.Y., Zhuang, Q.Q., Zhu, L.B., et al., 2016. Meta-analysis of brain iron levels of Parkinson's disease patients determined by postmortem and MRI measurements. Sci. Rep. 6, 36669.
Wang, Y., Chen, Y., Wu, D., et al., 2018. STrategically Acquired Gradient Echo (STAGE) imaging, part II: correcting for RF inhomogeneities in estimating T1 and proton density. Magn. Reson. Imag. 46, 140–150.
Wharton, S., Bowtell, R., 2010. Whole-brain susceptibility mapping at high field: a comparison of multiple- and single-orientation methods. NeuroImage 53 (2), 515–525.
Wharton, S., Bowtell, R., 2012. Fiber orientation-dependent white matter contrast in gradient echo MRI. Proc. Natl. Acad. Sci. U. S. A. 109 (45), 18559–18564.
Wharton, S., Bowtell, R., 2013. Gradient echo based fiber orientation mapping using R2* and frequency difference measurements. NeuroImage 83, 1011–1023.
Wharton, S., Bowtell, R., 2015. Effects of white matter microstructure on phase and susceptibility maps. Magn. Reson. Med. Off. J. Soc. Magn. Reson. Med./Soc. Magn. Reson. Med. 73 (3), 1258–1269.
Wieler, M., Gee, M., Martin, W.R., 2015. Longitudinal midbrain changes in early Parkinson's disease: iron content estimated from R2*/MRI. Park. Relat. Disord. 21 (3), 179–183.
Wilkinson, J., Di, X.M., Schonig, K., et al., 2006. Tissue-specific expression of ferritin H regulates cellular iron homoeostasis in vivo. Biochem. J. 395, 501–507.
Wisnieff, C., Ramanan, S., Olesik, J., Gauthier, S., Wang, Y., Pitt, D., 2015. Quantitative susceptibility mapping (QSM) of white matter multiple sclerosis lesions: interpreting positive susceptibility and the presence of iron. Magn. Reson. Med. Off. J. Soc. Magn. Reson. Med./Soc. Magn. Reson. Med. 74 (2), 564–570.
Wood, J.C., 2014. Use of magnetic resonance imaging to monitor iron overload. Hematol. Oncol. Clin. N. Am. 28 (4), 747–764 (vii).
Wood, J.C., Tyszka, J.M., Carson, S., Nelson, M.D., Coates, T.D., 2004. Myocardial iron loading in transfusion-dependent thalassemia and sickle cell disease. Blood 103 (5), 1934–1936.
Wood, J.C., Enriquez, C., Ghugre, N., et al., 2005. MRI R2 and R2* mapping accurately estimates hepatic iron concentration in transfusion-dependent thalassemia and sickle cell disease patients. Blood 106 (4), 1460–1465.
Wood, J.C., Otto-Duessel, M., Aguilar, M., et al., 2005. Cardiac iron determines cardiac T2*, T2, and T1 in the gerbil model of iron cardiomyopathy. Circulation 112 (4), 535–543.
Xia, S., Utriainen, D., Tang, J., et al., 2014. Decreased oxygen saturation in asymmetrically prominent cortical veins in patients with cerebral ischemic stroke. Magn. Reson. Imag. 32 (10), 1272–1276.
Xia, S., Zheng, G., Shen, W., et al., 2015. Quantitative measurements of brain iron deposition in cirrhotic patients using susceptibility mapping. Acta Radiol. 56 (3), 339–346.
Yablonskiy, D.A., Haacke, E.M., 1994. Theory of NMR signal behavior in magnetically inhomogeneous tissues: the static dephasing regime. Magn. Reson. Med. Off. J. Soc. Magn. Reson. Med./Soc. Magn. Reson. Med. 32 (6), 749–763.
Yablonskiy, D.A., Haacke, E.M., 1997. An MRI method for measuring T2 in the presence of static and RF magnetic field inhomogeneities. Magn. Reson. Med. Off. J. Soc. Magn. Reson. Med./Soc. Magn. Reson. Med. 37 (6), 872–876.
Yablonskiy, D.A., Sukstanskii, A.L., 2017. Effects of biological tissue structural anisotropy and anisotropy of magnetic susceptibility on the gradient echo MRI signal phase: theoretical background. NMR Biomed. 30 (4).
Yan, S.Q., Sun, J.Z., Yan, Y.Q., Wang, H., Lou, M., 2012. Evaluation of brain iron content based on magnetic resonance imaging (MRI): comparison among phase value, R2* and magnitude signal intensity. PLoS One 7 (2), e31748.
Yao, B., Li, T.Q., Gelderen, P., Shmueli, K., de Zwart, J.A., Duyn, J.H., 2009. Susceptibility contrast in high field MRI of human brain as a function of tissue iron content. NeuroImage 44 (4), 1259–1266.
Yu, H., Shimakawa, A., McKenzie, C.A., Brodsky, E., Brittain, J.H., Reeder, S.B., 2008. Multiecho water-fat separation and simultaneous R2* estimation with multifrequency fat spectrum modeling. Magn. Reson. Med. Off. J. Soc. Magn. Reson. Med./Soc. Magn. Reson. Med. 60 (5), 1122–1134.
Zhang, J., Zhang, Y., Wang, J., et al., 2010. Characterizing iron deposition in Parkinson's disease using susceptibility-weighted imaging: an in vivo MR study. Brain Res. 1330, 124–130.
Zhang, J., Chamberlain, R., Etheridge, M., et al., 2014. Quantifying iron-oxide nanoparticles at high concentration based on longitudinal relaxation using a three-dimensional SWIFT Look-Locker sequence. Magn. Reson. Med. Off. J. Soc. Magn. Reson. Med./Soc. Magn. Reson. Med. 71 (6), 1982–1988.
Zhang, Y., Gauthier, S.A., Gupta, A., et al., 2016. Quantitative susceptibility mapping and R2* measured changes during white matter lesion development in multiple sclerosis: myelin breakdown, myelin debris degradation and removal, and iron accumulation. AJNR Am. J. Neuroradiol. 37 (9), 1629–1635.
Zheng, W., Nichol, H., Liu, S., Cheng, Y.C., Haacke, E.M., 2013. Measuring iron in the brain using quantitative susceptibility mapping and X-ray fluorescence imaging. NeuroImage 78, 68–74.
Zhou, D., Liu, T., Spincemaille, P., Wang, Y., 2014. Background field removal by solving the Laplacian boundary value problem. NMR Biomed. 27 (3), 312–319.